Available online at www.sciencedirect.com
ScienceDirect
Comput. Methods Appl. Mech. Engrg. 362 (2020) 112843
Computer methods in applied mechanics and engineering
www.elsevier.com/locate/cma

A numerical simulation study of the dual role of 5α-reductase inhibitors on tumor growth in prostates enlarged by benign prostatic hyperplasia via stress relaxation and apoptosis upregulation

G. Lorenzo[a,*], T.J.R. Hughes[b], A. Reali[a], H. Gomez[c,d,e]

[a] *Dipartimento di Ingegneria Civile e Architettura, Università degli Studi di Pavia, Via Ferrata 3, 27100 Pavia, Italy*
[b] *Institute for Computational Engineering and Sciences, The University of Texas at Austin, 201 East 24th Street, C0200, Austin, TX 78712-1229, USA*
[c] *School of Mechanical Engineering, Purdue University, 516 Northwestern Avenue, West Lafayette, IN 47907, USA*
[d] *Weldon School of Biomedical Engineering, Purdue University, 206 S. Martin Jischke Drive, West Lafayette, IN 47907, USA*
[e] *Purdue Center for Cancer Research, Purdue University, 201 S. University Street, West Lafayette, IN 47907, USA*

Available online 24 January 2020

Abstract

5α-reductase inhibitors are regarded as a promising chemoprevention strategy to reduce the incidence and delay the progression of prostate cancer. Landmark clinical trials have shown the chemopreventive potential of these drugs, but they appear to be mostly effective in mild tumors and have also been correlated with a higher prevalence of advanced prostate cancer. Hence, the use of 5α-reductase inhibitors for prostate cancer chemoprevention has become a controversial issue. The effects of these drugs on prostate cancer growth remain incompletely understood, but they are thought to promote apoptosis in the tumor. Additionally, 5α-reductase inhibitors induce global prostate shrinkage, which decreases the tumor-inhibiting effect of the mechanical stress accumulated in prostatic tissue due to common prostate enlargement with age. Thus, the competition between this mechanical effect and apoptotic upregulation may explain the controversial outcomes of 5α-reductase inhibitors on prostate cancer. Here, we extend our mechanically-coupled model of prostate cancer growth by including the mechanical and apoptotic action of 5α-reductase inhibitors and explore their combined effect on an aggressive tumor *in silico*. Our simulations show that the apoptotic boost dominates in the first months of therapy but the long-term outcome of 5α-reductase inhibitors depends on its competition with a decrease in hydrostatic stress caused by prostate shrinkage, which favors tumor growth. By combining moderate or strong prostate shrinkage with mild or intense apoptotic upregulation, our simulations show different tumor growth dynamics ranging from long-term inhibition of prostate cancer growth to rapidly growing large tumors, which may evolve towards advanced disease. Thus, our proposed mechanism for the action of 5α-reductase inhibitors may contribute to resolve the controversy around the use of these drugs for chemoprevention and to gain insight on prostate cancer dynamics during its use. The computational technology used herein could also assist physicians to monitor prostatic tumors during 5α-reductase inhibitor therapy and enable the early identification of responders from non-responders in a patient-specific manner.

Keywords: Prostate cancer; Benign prostatic hyperplasia; Mathematical oncology; Isogeometric analysis; Phase field; Mechanical coupling

* Corresponding author.
E-mail address: guillermo.lorenzo@unipv.it (G. Lorenzo).

https://doi.org/10.1016/j.cma.2020.112843
0045-7825/

1. Introduction

Benign prostatic hyperplasia (BPH) and prostate cancer (PCa) are two major urogenital pathologies among aging men that often coexist in the same patient [1]. BPH consists of the progressive enlargement of the prostate with age and has an increasing prevalence from approximately 50% of men in their fifties to about 80% of men in their eighties [1–3]. This pathology only develops in the central gland (CG) of the prostate, which aggregates the most internal zones of the organ and is surrounded by the peripheral zone (PZ) [1,4,5]. Although the mechanisms explaining the origin of BPH are not fully understood, current evidence points toward a disruption of androgen-regulated homeostasis, which favors proliferative processes over cell death by apoptosis [1,3,6,7]. The growing tissue in BPH usually provokes bothersome lower urinary tract symptoms due to the compression of the urethra and bladder outlet obstruction. PCa is the second most common and the fifth most lethal tumor among men worldwide [8]. The vast majority of PCa cases originate in glandular epithelial tissue of the prostate, approximately 70% in the PZ and 30% in the CG [1]. PCa arises due to the accumulation of genetic alterations that confer cancerous cells an aberrant and competitive behavior, characterized by overproliferation and high invasiveness. PCa initially grows within the prostate zone where it originated, gradually progressing towards a more malignant cancer that may invade other nearby or distant tissues [1,9]. However, the current clinical management of PCa enables the detection and effective treatment of most prostatic tumors at an early stage, when they are still localized within the prostate [1,10].

Androgens play a pivotal role in the development, function, and pathogenesis of the prostate [1,3,6,7]. The principal androgen in the prostate is dihyrotestosterone (DHT), which is synthesized from testosterone by the enzymatic action of 5α-reductase within prostatic cells. There are three known isoenzymes of 5α-reductase: type 1, which is mainly present in skin and liver, but also exists in the prostate; type 2, which is present mainly in the prostate and male genital tissues; and type 3, which has been recently identified and is also expressed in several tissues, including the prostate [6,7,11]. The conversion of testosterone to DHT is mostly regulated by isoenzymes 1 and 2. DHT is known to regulate key proliferative and apoptotic mechanisms involved in the initiation and progression of both BPH and PCa [3,6,7,12–14]. Additionally, the expression of 5α-reductase types 1 and 2 is increased in BPH tissue, with type 2 being the predominant form [15–17]. Both 5α-reductase isoenzymes 1 and 2 are also present in PCa, with increasing levels in more aggressive tumors [16–18]. However, in PCa 5α-reductase type 1 is the predominant form and reaches higher levels than in BPH and healthy tissue, whereas the levels of 5α-reductase type 2 are lower or similar. Hence, the inhibition of 5α-reductase isoenzymes to impede the production of DHT has become a common target in the clinical management of BPH [3,19,20] and a promising strategy for chemoprevention of PCa [12,13,21]. Currently, two 5α-reductase inhibitors (5ARIs) have been approved for medical use: finasteride, which inhibits 5α-reductase type 2, and dutasteride, which is a more recent drug that targets both type 1 and 2 isoenzymes.

The main effect of 5ARIs is the promotion of cellular atrophy and apoptosis in the epithelial compartment of prostatic tissue [22–27], which results in the global shrinkage of the prostate. Similar reductions have been observed in PZ and CG volumes [24,28]. Volumetric shrinkage relieves the compression along the urethra, which alleviates the lower urinary tract symptoms induced by BPH [29–31]. Additionally, 5ARIs uniquely prevent BPH progression and reduce the risk of surgical intervention and acute urinary retention over other medical options for BPH. 5ARIs work better in larger prostates, so they are only prescribed for patients with prostate volume larger than 30–40 cc presenting bothersome lower urinary tract symptoms [19,20,32]. 5ARIs work rather slowly, so combination with an $\alpha 1$-blocker to promptly relax smooth muscle in the prostate and bladder neck is recommended. Combined therapies also contribute to control BPH progression [19,20]. Dutasteride provides a more potent inhibition of 5α-reductase types 1 and 2, which translates into a higher decrease in DHT [19,33]. Still, current evidence shows that finasteride and dutasteride are equally effective in treating BPH symptoms [19,20,34].

The rationale for chemoprevention of PCa using 5ARIs lies in the key regulatory activity of DHT in tumor dynamics and the slow-developing natural history of prostatic tumors [12,13,21]. Both finasteride and dutasteride have been shown to reduce the incidence of PCa (primary chemoprevention) in two landmark clinical trials, PCPT and REDUCE, respectively [35–37]. However, a higher proportion of more advanced PCa cases was detected in the 5ARI arm of these studies. This unexpected outcome sparked a major debate in the medical community about the safety of 5ARIs for chemoprevention of PCa, which has not yet been resolved [13,21,38–40]. Initially, it was hypothesized that 5ARIs might directly induce high-grade PCa [35,38] or alter tumor histopathological features suggesting a more advanced disease [38,40], but posterior investigations suggest that only mild PCa cases are effectively inhibited by 5ARIs [21,38,40–42]. Prostate shrinkage induced by 5ARIs might have also favored the

detection of aggressive tumors by improving the performance of PSA, digital rectal examination, and standard biopsy [13,38,43,44]. Still, these biases do not fully explain why the proportion of advanced tumors was higher in the 5ARI arms of PCPT and REDUCE. 5ARIs have also been investigated to delay the progression of newly-diagnosed low-risk PCa (secondary chemoprevention). This strategy is receiving much attention because it may reduce the overtreatment of indolent tumors while addressing the lower urinary tract symptoms induced by coexisting BPH [45–48]. However, despite some promising results from a large clinical trial [48], most studies have raised controversy on the methods used to assess PCa progression or have rendered contradictory results [21,47,49–51].

The tumor-inhibiting effect of 5ARIs is thought to be driven chiefly by an increase in pro-apoptotic signaling [22,52–55], but the studies assessing biomarkers of tumor growth *in vivo* or on prostate surgical specimens are scarce and they usually involve few patients followed-up for short time prior to scheduled surgery for PCa. This has led to inconclusive and even contradictory results on the effects of 5ARIs on tumor dynamics [55–57]. The differences in apoptotic and proliferative markers observed in tumors treated with 5ARIs can be attributed to the complex effects of 5ARIs on androgen-regulated signaling and the variable and evolving phenotypes of prostatic tumors [13,14,54,58]. However, the 5ARI-induced prostate shrinkage can also dramatically alter the mechanical stress fields in the prostate, which are known to have a key influence in solid tumor dynamics and have been largely overlooked in clinical studies of PCa chemoprevention with 5ARIs [59–65]. Prostatic tumors originating in larger prostates are known to exhibit more favorable pathological features (e.g.: low volume, low aggressiveness, mild invasive behavior) [66–68]. This suggests that large prostates may exert a protective effect against PCa, but the underlying mechanisms are unknown. Recently, we proposed a mechanical explanation for this phenomenon: the mechanical stress accumulated by BPH over time impedes the growth of prostatic tumors in enlarged prostates [69]. According to this mechanism, the prostate shrinkage induced by 5ARIs could reduce the mechanical constraint on PCa, hence promoting tumor growth. Therefore, the chemopreventive outcome of 5ARIs would depend on the trade-off between this mechanical release due to volumetric shrinkage and the increase in apoptosis. The combination of these opposed effects may contribute to explain the variability in tumor response to 5ARIs, hence shedding light on the current controversy surrounding their potential for chemoprevention of PCa.

Here, we explore the combined outcome of mechanical and apoptotic effects of 5ARIs on prostatic tumors through a simulation study based on our mechanically-coupled model of PCa growth [69]. We explore different simulation scenarios by considering (1) a moderate or an intense law of 5ARI-induced prostate shrinkage extracted from literature data [29,31], and (2) no, mild, or strong 5ARI-induced apoptotic boost. We focus on aggressive tumors in order to gain insight into the underlying mechanisms that explain the controversial results observed in clinical trials with 5ARIs. In all cases, we simulate 2 years of tumor growth to capture both early and late effects of 5ARIs. Computational modeling of cancer growth is an emerging and promising field [70–72], which has been contributing to increasing the knowledge on these pathologies and providing personalized technologies to assist physicians in their clinical management, e.g.: by early identification of aggressive tumors or designing optimal treatment plans [69,73–79]. The inclusion of mechanical effects in computational models of cancer has been shown to improve their performance [69,77–82]. Additionally, the use of a patient-specific geometric model of the tumor and harboring organ contributes to accurately predict tumor growth, anticipate disease-specific complications, and refine treatment strategies. In mechanically-coupled models, a patient-specific anatomic model is also essential to obtain a realistic estimation of mechanical displacements and stresses. Thus, we use the original geometry of a patient's prostate and tumor extracted from magnetic resonance (MR) images. To handle the computational challenges arising from the model equations and the complex geometries of both prostate and tumor, our numerical methods rely on Isogeometric Analysis (IGA) [83,84].

The structure of the paper is as follows. Section 2 briefly describes the source and contents of the patient data used in this study. In Section 3, we present the assumptions and equations of our mechanically-coupled model of localized PCa growth. Section 4 outlines the computational methods used to solve the model equations, construct the prostate mesh, visualize results, and estimate the dynamic parameters to characterize the prostate shrinkage laws due to the mechanical action of 5ARIs. Section 5 presents the simulation results. Finally, in Section 6 we discuss our results, draw conclusions, and outline future lines of work.

2. Patient data

Anonymized patient data were obtained from the 3T multiparametric MR imaging dataset that is publicly available at the Initiative for Collaborative Computer Vision Benchmarking webpage (i2cvb.github.io/) [85].

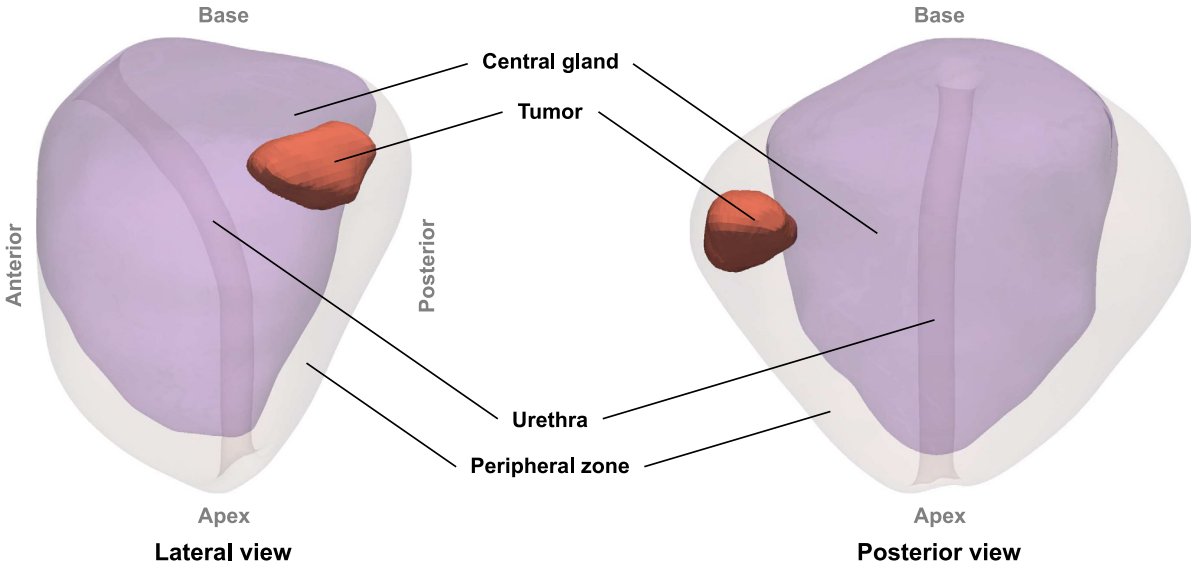

Fig. 1. Patient-specific local anatomy of the prostate. The volumes of the prostate, CG, and PZ at MRI date are 52.8 cc, 33.1 cc, and 19.7 cc, respectively. The major diameters of the prostate at MRI date have a length of 53.5 mm, 38.4 mm, and 52.0 mm in lateral, anteroposterior, and craniocaudal directions, respectively. The initial volume of the patient's tumor is approximately 0.6 cc.

Institutional review board approval and informed consent were not required for this study. Details of the patient cohort and image acquisition have been previously reported [86]. For each patient with biopsy-confirmed PCa, the database provides T2-weighted MR images, dynamic contrast enhanced MR images, diffusion weighted MR images, MR spectroscopic images, apparent diffusion coefficient maps, and the segmentations of the prostate, the PZ, the CG, and the tumor by an experienced radiologist. In our research, we used the data corresponding to a patient aged 54 years at imaging date who had a large prostate (52.8 cc) and a localized tumor in the left superior PZ. The local anatomy of this patient's prostate is depicted in Fig. 1.

3. Mathematical model

In [69], we developed a mechanically-coupled model to describe the growth of localized PCa in a patient's prostate deformed by the tumor mass effect and BPH. Here, we use this model but we drop the equation for PSA dynamics because 5ARIs are known to alter PSA production in a complex manner [19]. As discussed in Section 6, we believe the effects of 5ARIs on PSA dynamics deserves further research and here we focus on the mechanic and apoptotic effects of these drugs on PCa growth. Thus, our model is composed of the following equations:

$$\frac{\partial \phi}{\partial t} = \nabla \cdot \left(M\left(\boldsymbol{\sigma}\right) D_{\phi} \nabla \phi \right) + M\left(\boldsymbol{\sigma}\right) \left(\chi s - A\phi - \frac{1}{\tau} \frac{dF(\phi)}{d\phi} \right) \tag{1}$$

$$\frac{\partial s}{\partial t} = D_s \Delta s + S - \delta \phi - \gamma_s s \tag{2}$$

$$\nabla \cdot \boldsymbol{\sigma} = \mathbf{0} \tag{3}$$

Eq. (1) governs tumor dynamics. We use the phase-field method to describe the coupled evolution of healthy and cancerous tissue [87,88]. Hence, we define an order parameter ϕ that smoothly varies in $[0, 1]$ along a thin diffuse interface between lower values in healthy tissue and higher values within the tumor. The function $F\left(\phi\right) = 16\phi^2 \left(1 - \phi\right)^2$ is a double-well potential, which enables the stable coexistence of healthy and tumor tissue in our model. The last two terms in Eq. (1) represent tumor growth driven by a generic nutrient s and apoptosis (i.e. programmed cell death), respectively. We assume that the generic nutrient s follows the reaction–diffusion dynamics described in Eq. (2), where the reactive terms respectively represent nutrient supply, nutrient consumption by the tumor, and a natural decay.

The function $M(\boldsymbol{\sigma})$ in Eq. (1) models the inhibitory effect of mechanical stress on tumor growth [59–64] with a coefficient that exponentially decays as mechanical stress fields intensify in the tumor neighborhood. This modeling paradigm has been used in previous mechanically-coupled models to decrease tumor cell mobility or net proliferation, resulting in superior predictions on breast and brain cancer evolution [71,77–82]. Mechanical stress can be written as the sum of hydrostatic stress σ_h (defined in Eq. (5)), which tends to change the volume of a deformable body, and deviatoric stress, which tends to distort it [89]. The definition of $M(\boldsymbol{\sigma})$ in previous mechanically-coupled tumor growth models relied on the Von Mises stress σ_v (defined in Eq. (6)), which accounts for the distortional strain energy around the tumor [77,78,80]. However, σ_v does not capture hydrostatic stress σ_h, which characterizes the mechanical stress state within a region of growing tissue, such as a tumor or the CG developing BPH [60,62,63]. Additionally, σ_h may further increase globally during tumor growth and BPH due to the confinement of the prostate within the pelvic region. Thus, we define $M(\boldsymbol{\sigma})$ with a combination of σ_v and σ_h following a similar approach to multiaxial stress-based criteria, i.e.,

$$M(\boldsymbol{\sigma}) = e^{-\beta_1(\sigma_v+\beta_2|\sigma_h|)}, \tag{4}$$

where

$$\sigma_h = \frac{1}{3}\boldsymbol{\sigma} : \mathbf{I} = \frac{1}{3}\left(\sigma_{11}+\sigma_{22}+\sigma_{33}\right), \tag{5}$$

$$\sigma_v = \sqrt{\sigma_{11}^2+\sigma_{22}^2+\sigma_{33}^2-\sigma_{11}\sigma_{22}-\sigma_{22}\sigma_{33}-\sigma_{33}\sigma_{11}+3\left(\sigma_{12}^2+\sigma_{23}^2+\sigma_{13}^2\right)}, \tag{6}$$

σ_{ij} with $i, j = 1, 2, 3$ are the components of the stress tensor $\boldsymbol{\sigma}$, $\mathbf{I}$ is the second-order identity tensor, and β_1 and β_2 are constants that were calibrated to match empirical observations in previous studies of tumor growth [59–64,78–80]. The mechanical stresses generated by solid cancer growth are normally compressive within the tumor and tensile around it, even though they may become predominantly compressive if the confinement of the tumor increases [62,63,65,69]. In Eq. (4), we use the absolute value of hydrostatic stress because both tensile and compressive tumor-induced mechanical stresses have been found to impede cancer growth *in vivo* [62,63].

In Eq. (3) we assumed quasistatic linear elasticity because PCa and BPH are slowly developing pathologies that allow neglecting inertial effects [1]. Linear elasticity has been widely adopted to describe the mechanical deformation of living tissue hosting a slowly growing tumor over short time scales ($t \sim 1$ year) [77–82,89–93]. This paradigm has been observed to provide an acceptable approximation of the mechanical stress fields generated during cancer growth. The PZ and the CG of the prostate show significant differences in their histological composition: while the CG has a larger and denser stromal component, the PZ has more abundant glandular elements with sparsely interwoven smooth muscle [1,5,94]. Additionally, BPH tends to render the CG denser and more compact [1,95]. Hence, the CG is normally stiffer than the PZ in PCa and BPH patients [96–99]. Tumors generate internal compressive hydrostatic stress and exert outward forces acting on the tumor border [62,63,65,100], so we modeled the tumor mass effect with the pressure load

$$p_{tumor} = -\kappa\phi \tag{7}$$

This assumes that κ is the magnitude of a constant compressive pressure, which is admissible over short simulation times [77–80,82,91,92]. While BPH is usually modeled with an exponential function of time, the slow growth rates of this condition justify the use of a linear approximation over periods of time in the order of a few years [101–103]. Thus, we model the load imposed by BPH with another pressure term acting exclusively in the CG and given by

$$p_{BPH} = -K\hat{v}_{BPH}(t)\,\mathcal{H}_{CG}(\mathbf{x}), \tag{8}$$

where K is the bulk modulus and $\mathcal{H}_{CG}(\mathbf{x})$ is a Heaviside function with value 1 in the CG and 0 elsewhere. The function $\hat{v}_{BPH}(t)$ describes the volumetric deformation induced by BPH as

$$\hat{v}_{BPH}(t) = \begin{cases} g_{BPH}t, & \text{if } t < t_{5ARI} \\ g_{BPH}t_{5ARI}, & \text{if } t \geq t_{5ARI} \end{cases} \tag{9}$$

where g_{BPH} represents the linear rate of unit volumetric expanse of the CG due to BPH and t_{5ARI} denotes the time at which the patient starts taking the 5ARI. Notice that Eq. (9) assumes that 5ARIs inhibit BPH volumetric growth right after treatment initiation [1,3,19,24,28–31]. We model the mechanical effect associated with the reduction of prostate volume by 5ARI action with the pressure load

$$p_{5ARI} = K\hat{v}_{5ARI}(t), \tag{10}$$

in which

$$\hat{v}_{5ARI}(t) = \hat{v}_{5ARI,\infty}\left(1 - e^{-(t-t_{5ARI})/\tau_{5ARI}}\right)\mathcal{H}(t - t_{5ARI}) \tag{11}$$

where $\hat{v}_{5ARI,\infty}$ is the asymptotic maximal volumetric reduction of the prostate induced by 5ARI, τ_{5ARI} is a characteristic time of action of the 5ARI, and $\mathcal{H}(t - t_{5ARI})$ is a Heaviside function [24,28–31]. Therefore, we model prostatic tissue as a linear elastic, heterogeneous, isotropic material that follows the constitutive equation given by

$$\boldsymbol{\sigma} = \mathcal{C} : \boldsymbol{\nabla}^s\mathbf{u} + (p_{tumor} + p_{BPH} + p_{5ARI})\,\mathbf{I} = \lambda\,(\boldsymbol{\nabla}\cdot\mathbf{u})\,\mathbf{I} + 2\mu\boldsymbol{\nabla}^s\mathbf{u} - \kappa\phi\mathbf{I} - K\left(\hat{v}_{BPH}\mathcal{H}_{CG}(\mathbf{x}) - \hat{v}_{5ARI}\right)\mathbf{I} \tag{12}$$

where $\boldsymbol{\sigma}$ is the stress tensor, $\mathcal{C}$ is the fourth-order linear elasticity tensor, $\boldsymbol{\nabla}^s\mathbf{u}$ denotes the symmetric gradient of the displacement field (i.e., the strain tensor in linear elasticity $\boldsymbol{\epsilon} = (\boldsymbol{\nabla}\mathbf{u} + \boldsymbol{\nabla}\mathbf{u}^{\mathrm{T}})/2$), λ and μ are the Lamé constants, $\mathbf{u}$ is the displacement vector, and $\mathbf{x}$ is the position vector. The Lamé constants and the bulk moduli of the CG and the PZ were computed from the corresponding Young's modulus and Poisson's ratio reported in the literature [69,79,92,96–99] in the usual way [89].

We computed tumor volume V_ϕ as in [73,104]:

$$V_\phi = \int_\Omega \phi\, d\Omega \tag{13}$$

where Ω is the patient's prostate geometry as extracted from T2-weighted MR images.

To focus on localized PCa, we imposed zero-valued Dirichlet conditions for ϕ all over the prostate boundary Γ and set natural boundary conditions for s. Prostate confinement within the pelvic region [1] was modeled with Winkler-inspired boundary conditions on the external surface of the prostate Γ_{ext}, while a traction-free condition was imposed along the urethra Γ_u, i.e.,

$$\begin{aligned} \boldsymbol{\sigma}\mathbf{n} &= -k_w\mathbf{u} \quad \text{in } \Gamma_{ext} \\ \boldsymbol{\sigma}\mathbf{n} &= \mathbf{0} \quad\;\; \text{in } \Gamma_u \end{aligned} \tag{14}$$

where $\mathbf{n}$ is the outer normal vector to Γ and k_w is constant.

We set $t = 0$ at the date of the patient's MR. The initial condition of the phase field ϕ_0 was obtained as the L^2-projection of the provided tumor segmentation, which was extracted from the patient's T2-weighted MR images and mapped over the quadrature points. The initial nutrient concentration s_0 was approximated with a linear function of ϕ_0 as in [104].

At the imaging date, the patient's prostate has already been experiencing a deformation caused by BPH over years. As we are using linear elasticity, we invoke the Principle of Superposition and split the total displacement field as $\mathbf{u} = \mathbf{u}^0 + \mathbf{u}^1$, where $\mathbf{u}^0$ are the displacements produced by the history of BPH before the onset of the simulation (i.e., prior to MR date) and $\mathbf{u}^1$ are the displacements generated by BPH and PCa during the simulation (i.e., after the MR date). We accordingly split the total stress tensor as $\boldsymbol{\sigma} = \boldsymbol{\sigma}^0 + \boldsymbol{\sigma}^1$. Hence, we can set $\mathbf{u}^1_0 = \mathbf{0}$ and use Eq. (3) to compute $\mathbf{u}^1$ during the simulations, from which we can obtain $\boldsymbol{\sigma}^1$ using Eq. (12). To account for the mechanical inhibition of PCa growth due to a history of BPH, we need to estimate $\mathbf{u}^0$ to obtain $\boldsymbol{\sigma}^0$ and use it as a prestress to compute $M(\boldsymbol{\sigma})$ in Eq. (1). We assumed that the volume of the patient's prostate was 20 cc at age 40 [1,2] and leveraged Eq. (3) with a negative value for g_{BPH} in Eq. (12) to approximate the undeformed, healthy state of our patient's prostate according to standard anatomical features [1]. Because we are using linear elasticity, it suffices to reverse the sign of the obtained displacements to yield $\mathbf{u}^0$ and then calculate $\boldsymbol{\sigma}^0$ as

$$\boldsymbol{\sigma}^0 = \lambda\left(\boldsymbol{\nabla}\cdot\mathbf{u}^0\right)\mathbf{I} + 2\mu\boldsymbol{\nabla}^s\mathbf{u}^0 - Kg_{BPH}t^0\mathcal{H}_{CG}(\mathbf{x})\,\mathbf{I} \tag{15}$$

where g_{BPH} is now positive and $t^0 = 14$ years.

4. Computational methods

To perform the numerical simulations, we developed algorithms based on the concept of Isogeometric Analysis (IGA) [83,84]. This rapidly growing and cutting-edge technology can be seen as a generalization of the classic Finite Element Analysis [105]. Instead of using standard piecewise polynomials, IGA leverages richer functions coming from computer graphics and computational geometry, such as B-splines [83,84,106], Non-Uniform Rational B-splines (NURBS) [83,84,106], and T-splines [107]. Isogeometric methods can leverage the exact geometry of the

problem, provide enhanced accuracy per degree of freedom, and enable higher-order global continuity (C^{p-1} for spline spaces with polynomial degree p) [84,108]. Thus, IGA is an ideal technology to handle the nonlinearity of our tumor growth problem, the complex anatomy of the prostate, and the intricate morphologies of PCa. Additionally, the higher-order global continuity enables the pointwise computation of mechanical stress fields, which is a key advantage for the study presented herein. Here, we manually implemented the model described in Section 3 by extending our in-house isogeometric codes to simulate PCa growth. These codes were built following the general directions in [84].

4.1. Spatial discretization

The strong form of our mechanically-coupled model of PCa growth is composed of Eqs. (1)–(3). We approximated its solution by means of an isogeometric Bubnov–Garlerkin approach using a three-dimensional quadratic NURBS space, which we denote by $\mathcal{N}$. This functional space is spanned by the corresponding three-dimensional quadratic standard NURBS basis $\mathsf{N} = \{N_A\}_{A=1,\dots,n_f}$, where n_f is the number of functions in the basis (see [84] for further details). We will only work with free-flux, Winkler-inspired, or zero-valued Dirichlet boundary conditions. Thus, let $\mathcal{V}$ denote the trial solution and weighting function spaces, which are assumed to be identical. The space $\mathcal{V}$ is a subset of H^1, the Sobolev space of square integrable functions with square integrable first derivatives. Let us define the discrete space $\mathcal{V}^h = \mathcal{N}$, which is a subset of $\mathcal{V}$. Let ϕ^h, s^h, and $\left\{u_i^h\right\}_{i=1,2,3}$ be an approximation to our solution fields in $\mathcal{V}^h$, such that $\mathbf{u}^h = \left\{u_i^h\right\}_{i=1,2,3}$. We also define v^h, w^h, and $\left\{r_i^h\right\}_{i=1,2,3}$ in $\mathcal{V}^h$ as the weighting functions respectively associated to Eqs. (1)–(3), such that $\mathbf{r}^h = \left\{r_i^h\right\}_{i=1,2,3}$. Then, the corresponding variational problem to Eqs. (1)–(3) over the finite dimensional space $\mathcal{V}^h$ can be stated as follows: find $\phi^h, s^h, u_i^h \in \mathcal{V}^h \subset \mathcal{V}$ such that $\forall v^h, w^h, r_i^h \in \mathcal{V}^h \subset \mathcal{V}$

$$\int_\Omega v^h \frac{\partial \phi^h}{\partial t} d\Omega + \int_\Omega M\left(\boldsymbol{\sigma}^h\right) D_\phi \nabla v^h \cdot \nabla \phi^h d\Omega - \int_\Omega M\left(\boldsymbol{\sigma}^h\right) v^h \left(\chi s^h - A\phi^h - \frac{1}{\tau}\frac{dF\left(\phi^h\right)}{d\phi}\right) d\Omega = 0 \tag{16}$$

$$\int_\Omega w^h \frac{\partial s^h}{\partial t} d\Omega + \int_\Omega D_s \nabla w^h \cdot \nabla s^h d\Omega - \int_\Omega w^h \left(S - \delta\phi^h - \gamma_s s^h\right) d\Omega = 0 \tag{17}$$

$$\int_\Omega \nabla^s \mathbf{r}^h : \mathcal{C} : \nabla^s \mathbf{u}^h \, d\Omega + \int_{\Gamma_{ext}} k_w \, \mathbf{r}^h \cdot \mathbf{u}^h \, d\Gamma - \int_\Omega \left(\kappa\phi^h + K\left(\hat{v}_{BPH}\mathcal{H}_{CG}\left(\mathbf{x}\right) - \hat{v}_{5ARI}\right)\right) \nabla \cdot \mathbf{r}^h d\Omega = 0 \tag{18}$$

Here, the approximated solution fields ϕ^h, s^h and $\mathbf{u}^h = \left\{u_i^h\right\}_{i=1,2,3}$ are defined as

$$\phi^h(\mathbf{x}, t) = \sum_{A=1}^{n_f} \phi_A(t) N_A(\mathbf{x}) \tag{19}$$

$$s^h(\mathbf{x}, t) = \sum_{A=1}^{n_f} s_A(t) N_A(\mathbf{x}) \tag{20}$$

$$\mathbf{u}^h(\mathbf{x}, t) = \sum_{A=1}^{n_f} \mathbf{u}_A(t) N_A(\mathbf{x}) \tag{21}$$

where the coefficients ϕ_A, s_A and $\mathbf{u}_A = \left\{u_{i,A}\right\}_{i=1,2,3}$ are the so-called control variables in the context of IGA. The weighting functions v^h, w^h, and $\mathbf{r}^h = \left\{r_i^h\right\}_{i=1,2,3}$ are defined analogously.

4.2. Time integration and numerical solvers

Because Eqs. (16) and (17) are dynamic and Eq. (18) is quasistatic, we chose a staggered approach to solve our model equations. Hence, we first computed tumor growth by solving Eqs. (16) and (17), and then we updated the displacements by solving Eq. (18). Because the deformation of the prostate in this study was slow overall, we only resolved the quasistatic mechanical equilibrium every two time steps to save time in our computations (comparison to solving mechanical equilibrium in every time step did not show significant differences). Time integration of Eqs. (16) and (17) was carried out with the generalized-α method [109,110]. The application of the generalized-α

method to Eqs. (16) and (17) led to a nonlinear problem at each time step, which we linearized by means of the Newton–Raphson method. The resulting linear system was then solved using the GMRES algorithm [111] with a diagonal preconditioner. The parameters of the generalized-α method were set as in [112]. We chose a constant time step $\Delta t = 0.002$ years for all the simulations in this study. The quasistatic elastic problem in Eq. (18) was also solved by means of the preconditioned GMRES algorithm. All integrals were calculated with standard Gaussian quadrature using three points per parametric direction [84].

4.3. Construction of the prostate mesh

The precise construction of patient-specific solid anatomic NURBS models is a rich subject [113,114]. Here, we exploited the topological equivalence between the geometries of a solid torus and the human prostate by leveraging a parametric mapping algorithm to deform a solid torus NURBS model to match with a surface model of the patient's prostate [115–117]. We used 3DSlicer [118] to construct a triangular surface model of the patient's prostate from the contours of the organ and the urethra drawn on the T2-weighted MR images, using the provided prostate segmentation as guidance. We manually adapted these contours to best capture the anatomy of the prostate as seen in axial, sagittal, and coronal planes. Because this surface was too coarse and rough, we exported it to MeshLab [119] for smoothing. The resulting prostate surface model was then checked again over the original T2-weighted MR images to assess the coherence with the observed prostate anatomy.

We used a polar discretization for the torus and the prostate [84]. The corresponding initial solid NURBS meshes had $32 \times 32 \times 8$ elements along the toroidal direction, the cross-section circumferential direction, and the cross-section radial direction, respectively. We globally refined the prostate mesh to $256 \times 256 \times 64$ elements by utilizing standard knot insertion [84] to ensure high accuracy in our simulations.

To define heterogeneous material properties, we flagged the quadrature points lying in the CG by mapping the segmentation of this prostatic region provided with the patient's imaging data (see Section 2).

4.4. Visualization

We visualized and explored the results of our simulations using ParaView [120]. We represented the tumor with the isovolume $\phi \geq 0.5$, which enabled us to easily analyze tumor growth and to locate its position in displacement and mechanical stress fields. The mechanical stress fields were computed pointwise thanks to the C^1-continuous spline basis used for the geometry and displacement discretization (see Section 4.1). By leveraging appropriate geometric filters available in ParaView, we isolated regions of interest in the mechanical stress fields of our simulations. The stress values reported in Section 5 best describe the corresponding mechanical stress fields within each region of interest.

4.5. Estimation of the dynamic parameters of 5ARI mechanical effects

To estimate the parameters $\hat{v}_{5ARI,\infty}$ and τ_{5ARI} in Eq. (11), we used available data in the literature from two landmark clinical trials of finasteride [29] and dutasteride [31] for the treatment of BPH symptoms. Data from the finasteride study was used to parameterize a moderate prostate shrinkage law, while data from the trial with dutasteride enabled us to parameterize a strong prostate volume shrinkage law. Nevertheless, note that both drugs have been reported to provide approximately the same average prostate volume reduction and that their action varies from patient to patient as well as with respect to the baseline prostate volume [19,29–32,34].

First, we used an equation like Eq. (11) to describe the empirical 5ARI-induced prostate volume shrinkage reported in those studies, i.e.,

$$\hat{v}_{5ARI}^{data}(t) = \hat{v}_{5ARI,\infty}^{data}\left(1 - e^{-(t-t_{5ARI})/\tau_{5ARI}^{data}}\right)\mathcal{H}(t - t_{5ARI}) \tag{22}$$

We parameterized this equation by solving a nonlinear least-squares problem using the trust-region method. We set $t_{5ARI} = 0$ and Table 1 shows the initial values, the lower bounds, and the upper bounds to fit $\hat{v}_{5ARI,\infty}^{data}$ and τ_{5ARI}^{data}. We assessed the goodness of fit with the R^2 and the root mean squared error (RMSE). We also computed the 95% confidence bound of the fit. These calculations were performed in MATLAB (Release R2017b, The Mathworks, Inc., Natick, Massachusetts, US) using the Curve Fitting Toolbox. The corresponding results are depicted in Fig. 2.

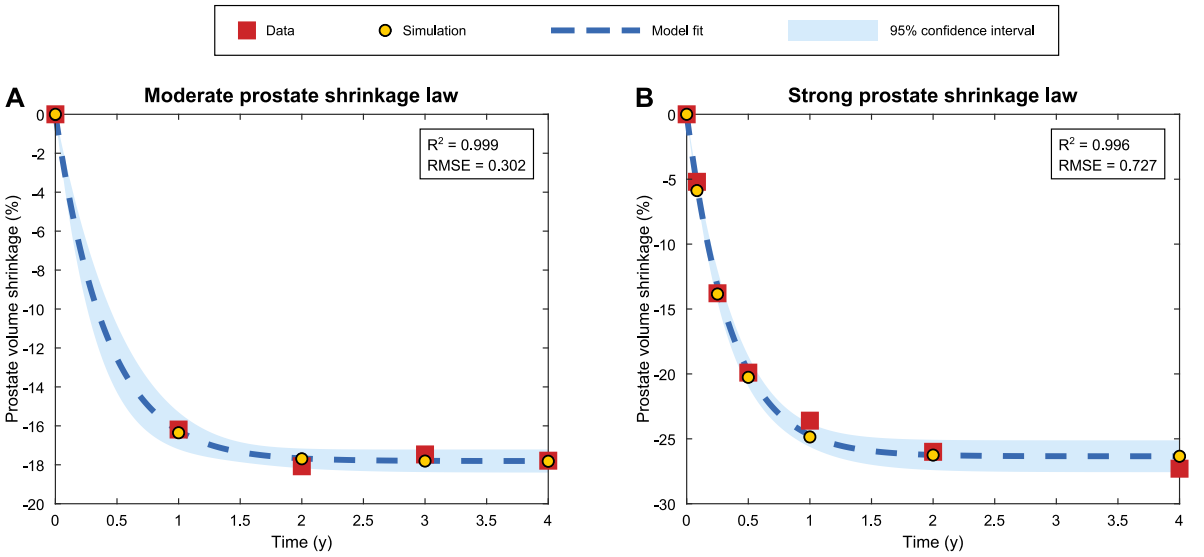

Fig. 2. Parameterization of the empirical 5ARI-induced prostate shrinkage laws used in this study using data from the literature. Each plot shows the progressive volumetric decrease of the prostate relative to the baseline at $t = 0$. (A) Moderate prostate shrinkage law obtained from the data reported in [29], for which $\hat{v}^{data}_{5ARI,\infty} = -17.81\%$ and $\tau^{data}_{5ARI} = 0.41$ years. (B) Strong prostate shrinkage law obtained from the data reported in [31], for which $\hat{v}^{data}_{5ARI,\infty} = -26.34\%$ and $\tau^{data}_{5ARI} = 0.36$ years. Data from the literature are plotted with red squares. Prostate volumes obtained in simulations with the patient data in this study using the corresponding values of $\hat{v}_{5ARI,\infty}$ and τ_{5ARI} (see Table 2) are represented using yellow circles with black contour at the same time points as data.

Table 1
Initial values and bounds for the trust-region algorithm used to fit the dynamic parameters characterizing the mechanical effects of 5ARIs.

Parameter	Initial value	Lower bound	Upper bound
$\hat{v}^{data}_{5ARI,\infty}$	-0.19	-0.50	-0.05
τ^{data}_{5ARI} (years)	0.40	0.01	1

Then, we made $\tau_{5ARI} = \tau^{data}_{5ARI}$ and iteratively resolved Eq. (3) to estimate $\hat{v}_{5ARI,\infty}$ departing from $\hat{v}_{5ARI,\infty} = \hat{v}^{data}_{5ARI,\infty}$. We only leveraged the mechanical effects of BPH as given by Eq. (15) and the mechanical effects of the corresponding 5ARI following Eq. (22) in the constitutive equation of the prostatic tissue (Eq. (12)). We set a tolerance of 0.1% for the relative error of the asymptotic prostate volume shrinkage obtained in simulations with respect to the corresponding $\hat{v}^{data}_{5ARI,\infty}$. The estimated values of $\hat{v}_{5ARI,\infty}$ and τ_{5ARI} for each 5ARI-induced prostate shrinkage law, i.e., moderate and strong, are reported in Table 2. Final volumetric shrinkage computed via simulation at the same times as the original data from [29,31] for each volumetric deformation law is also depicted in Fig. 2 (yellow circles with black contour).

5. Simulation study

5.1. Simulation setup

We ran four series of simulations in this study, as follows:

1. Simulations of the mechanical deformation of the prostate under the shrinking effects of 5ARIs without considering the tumor.
2. Simulation of tumor growth without the effects of 5ARIs. This simulation provides the reference dynamics to be compared against PCa growth observed under the mechanical and apoptotic effects of 5ARIs. In other words, this simulation serves as *in silico control*.

Table 2
Parameters of the mechanically-coupled model.

Parameter	Notation	Value
Tumor dynamics		
Mechanotransductive constant 1	β_1	0.80 1/kPa
Mechanotransductive constant 2	β_2	1.50
Diffusivity of the phase field	D_ϕ	200 mm^2/year
Time scale for the phase field	τ	0.01 years
Nutrient-induced tumor growth rate	χ	600 L/(g year)
Apoptosis rate	A	600 1/year
Nutrient dynamics		
Nutrient diffusivity	D_s	$5.47 \cdot 10^3$ mm^2/year
Nutrient supply	S	2.70 g/(L day)
Nutrient consumption rate	δ	2.75 g/(L day)
Nutrient natural decay rate	γ_s	1000 1/year
Mechanical problem		
Young modulus of the PZ	E_{PZ}	3 kPa
Poisson ratio of the PZ	ν_{PZ}	0.4
Young modulus of the CG	E_{CG}	6 kPa
Poisson ratio of the CG	ν_{CG}	0.4
Tumor-induced pressure load	κ	2.50 kPa
Rate of BPH-induced CG enlargement	g_{BPH}	0.12
Winkler-inspired boundary condition constant	k_w	0.23 kPa/mm
Moderate volumetric shrinkage law		
Asymptotic volumetric shrinkage	$\hat{v}_{5ARI,\infty}$	−0.24
Characteristic time	τ_{5ARI}	0.41 years
Strong volumetric shrinkage law		
Asymptotic volumetric shrinkage	$\hat{v}_{5ARI,\infty}$	−0.36
Characteristic time	τ_{5ARI}	0.36 years

3. Simulations of tumor growth exclusively under the mechanical effects of 5ARIs using both prostate shrinkage laws from Section 4.5. Thus, these simulations inherently assume that 5ARIs do not alter tumor apoptosis.
4. Simulations of tumor growth under both the mechanical and apoptotic effects of 5ARIs. We considered each prostate shrinking law from Section 4.5 and assumed either a mild or an intense upregulation of apoptosis. In the context of our model, we introduced these apoptotic boosts as a permanent increase of 5% or 10% in parameter A in Eq. (1), respectively.

The simulations to study the mechanical effects of 5ARIs in enlarged prostates without tumor considered 4 years of treatment to match the time range in the literature data used for the parameterization of prostate shrinkage laws [29,31]. In all the simulations including PCa, the total simulated time was 2 years to capture potential differences between early and late effects of 5ARIs. Table 2 provides the values of the parameters of our mechanically-coupled model used in the simulations. Parameter selection for Eqs. (1) and (2) has been previously discussed [73]. In particular, we chose χ and A to represent an aggressive tumor for the purposes of this study, as stated in Section 1. Ref. [69] addresses the choice of the elastic parameters of the PZ and CG, the constants β_1 and β_2 in the definition of $M(\boldsymbol{\sigma})$ in Eq. (4), the tumor-induced pressure load κ, the rate of BPH-induced CG volumetric enlargement g_{BPH}, and the constant k_w in the Winkler-inspired boundary conditions for the patient considered in this study.

5.2. Mechanical deformation induced by 5ARIs on prostates enlarged by BPH

The simulated 5ARI-induced shrinkage of the patient's prostate accurately reproduced the temporal evolution observed in the literature for the two volumetric decrease laws tested, as shown in Fig. 2. The global prostate shrinkage translated into a displacement field $\mathbf{u}_1$ directed inwards the organ, which intensified as the prostate shrank and reached a steady state for long times paralleling the evolution of the prostate volume in Fig. 2. Fig. 3 depicts the magnitude of the displacement field $\mathbf{u}_1$ obtained for each prostate shrinkage law at $t = 4$ years. For the moderate prostate shrinkage law, the maximum magnitude of the displacement field $\mathbf{u}_1$ at $t = 1$ year, $t = 2$ years, and $t = 4$

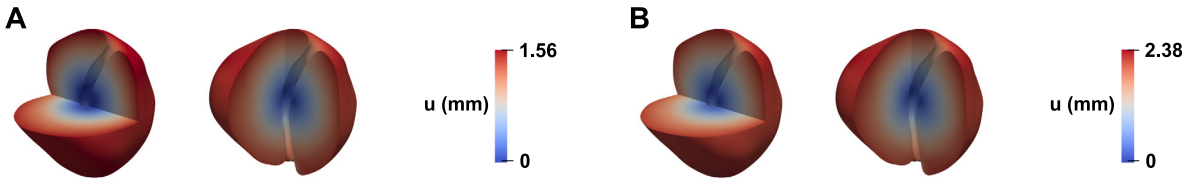

Fig. 3. Deformation of the prostate caused by 5ARI-induced shrinkage. (A) Anterior view of the magnitude of the displacement field vector $\mathbf{u}_1$ over the original anatomy at $t = 4$ years using the moderate prostate shrinkage law. (B) Anterior view of the magnitude of the displacement field vector $\mathbf{u}_1$ over the original anatomy at $t = 4$ years using the strong prostate shrinkage law.

years were 1.42 mm, 1.55 mm, and 1.56 mm, respectively. For the strong prostate shrinkage law, the maximum magnitude of the displacement $\mathbf{u}_1$ was 2.23 mm at $t = 1$ year, 2.37 mm at $t = 2$ years, and 2.38 mm at $t = 4$ years. These maximum values were registered on the external surface of the prostate. Conversely, the magnitude of the displacement field $\mathbf{u}_1$ had negligible values along the median segment of the urethra within the prostate.

Before the onset of the simulation, the mechanical stress field $\boldsymbol{\sigma}_0$ induced by the development of BPH over time was fundamentally characterized by large compressive stress in the CG (-2.7 to -2.3 KPa) and high Von Mises stress in the PZ, which decreased from the CG border (2.5 to 3.5 KPa) towards the prostate external surface (1.0 to 2.5 KPa). The Von Mises stress within the CG varied from negligible values at the innermost tissue (around 0.1 KPa) to values between 1.1 and 1.8 KPa close to the urethra and the border with the PZ. The hydrostatic stress within the PZ also took small values (-0.6 to -0.1 KPa). The expansion of the CG accumulated both Von Mises stress (4.00 to 8.00 KPa) and compressive hydrostatic stress (-4.0 KPa to -3.0 KPa) along the urethra. Both 5ARI prostate shrinkage laws progressively reduced the baseline compressive hydrostatic state and even introduced areas of tensile hydrostatic stress, while the Von Mises stress field remained virtually unaltered. The modification of the hydrostatic component of the total stress field $\boldsymbol{\sigma} = \boldsymbol{\sigma}_0 + \boldsymbol{\sigma}_1$ was more intense with the strong prostate shrinkage law (CG: -2.15 to -1.75 KPa, PZ: -0.20 to 0.45 KPa, urethra: -3.0 to -2.2 KPa for $t \geq 2$ years) than with the moderate prostate shrinkage law (CG: -2.4 to -2.0 KPa, PZ: -0.25 to 0.25 KPa, urethra: -3.5 to -2.5 KPa for $t \geq 2$ years).

5.3. Combined mechanical and apoptotic action of 5ARIs on PCa growth

The growth morphology of PCa was fundamentally massive in all simulations and tumors developed preferentially in anteriorposterior direction surrounding the CG. However, all tumors also developed lobular or finger-like structures in craniocaudal direction, especially during the second year of the simulation. Figs. 4, 5 and Videos S1–S2 show the growth of the patient's tumor in all the simulation scenarios outlined in Section 5.1. Additionally, Fig. 6 depicts the evolution of tumor volume in each simulation.

The *in silico* control tumor grew at a very low pace and only invaded the left superior aspect of the PZ. This tumor had a volume of 0.66 cc at $t = 1$ year and 1.18 cc at $t = 2$ years. When the 5ARI mechanical effects were introduced in the model, PCa exhibited an initial slow development that was almost identical to the control simulation. This initial phase was soon followed by a transition towards fast growth, approximately after $t = 0.5$ years. The simulation with the moderate prostate shrinkage law led to a larger tumor than the *in silico* control, measuring 1.02 cc at $t = 1$ year and 1.74 cc at $t = 2$ years. This tumor was still mostly contained within the left superior part of the PZ, only showing a minimal invasion of the inferior half of the left PZ at $t = 2$ years. The larger release of mechanical stress caused by the strong prostate shrinkage law led to the largest tumor volumes and fastest growth dynamics registered in this study, reaching 1.63 cc at $t = 1$ year and 3.15 cc at $t = 2$ years. This tumor was contained in the left superior PZ at $t = 1$ year, but by the end of the simulation it had expanded over the left inferior PZ and was starting to invade the right posterior PZ at median height.

The tumors in all the simulations including a 5ARI-induced apoptotic boost initially decreased in size until reaching a minimum volume and then proceeded to grow at diverse paces. We also observed that for each apoptotic boost, mild or intense, early tumor dynamics was invariant regardless of the prostate shrinkage law used in the simulation and that differences were only noticeable after the tumor reached a minimum volume. The initial PCa volumetric decrease was more intense if the apoptotic upregulation was larger, as shown in Fig. 6. For the moderate

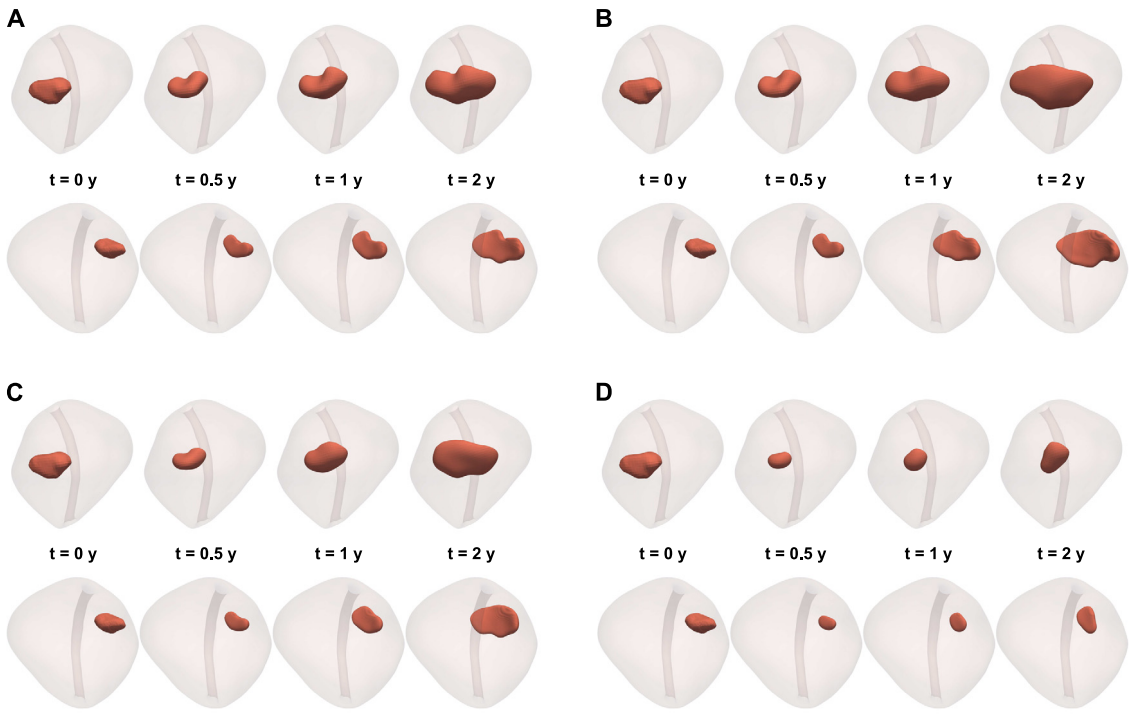

Fig. 4. Comparison of the mechanical and apoptotic effects of 5ARIs on the patient's tumor growth in different simulation scenarios using the moderate prostate shrinkage law. (A) No intake of 5ARI (*in silico* control). (B) Mechanical effects only (unaltered apoptosis). (C) Mechanical effects combined with 5% upregulation of tumor apoptosis. (D) Mechanical effects combined with 10% upregulation of tumor apoptosis. The top and bottom rows in each subfigure show a posterior and anterior view of the prostate, respectively.

prostate shrinkage law, this minimum tumor volume was 0.28 cc ($t = 0.43$ years) with the mild apoptotic boost and 0.12 cc ($t = 0.59$ years) with the intense apoptotic boost. For the strong prostate shrinkage law, the minimum tumor volume was 0.29 cc ($t = 0.36$ years) with the mild apoptotic boost and 0.14 cc ($t = 0.42$ years) with the intense apoptotic boost. Then, tumors grew larger and at a more rapid pace with the strong prostate shrinkage law than with the moderate prostate shrinkage law. For instance, in the simulations with a mild 5ARI-induced upregulation of apoptosis, the tumor volumes with the moderate and strong prostate shrinkage laws were 0.49 cc and 0.99 c at $t = 1$ year and 1.00 cc and 2.02 cc at $t = 2$ years, respectively. Likewise, when we considered a more intense upregulation of apoptosis, the tumor volumes with the moderate and strong prostate shrinkage laws were 0.15 cc and 0.42 cc at $t = 1$ year and 0.26 cc and 1.01 cc at $t = 2$ years, respectively. Three out of the four tests with 5ARI-induced apoptotic upregulation rendered a successful control of PCa volume with respect to the *in silico* control during the whole simulation: both cases using the moderate prostate shrinkage law and the case combining an intense apoptotic boost and the strong prostate shrinkage law. The simulation with mild apoptotic upregulation and the strong prostate shrinkage law only provided tumor volume control until $t = 0.74$ years. Afterwards, the tumor grew reaching a larger volume than in the simulation considering only mechanical effects with the moderate prostate shrinkage law, which constitutes the worst-case scenario for that volumetric reduction law. Additionally, the growth rate was faster than in the *in silico* control and by the end of the simulation this tumor slightly invaded the left inferior PZ and had a branch growing towards the right posterior PZ at upper median height. The simulation using an intense apoptotic boost plus the strong prostate shrinkage law and the simulation considering a mild apoptotic upregulation plus the moderate prostate shrinkage law produced similar tumor morphologies and dynamics. In both cases, the tumor grew exclusively in the left superior PZ. While the former case rendered a lower tumor volume minimum, for $t > 1.2$ years both simulations provided virtually the same tumor volume, which was somewhat lower than that of the *in silico* control. The best control in tumor volume was provided by the combination of the moderate prostate shrinkage law and the intense apoptosis upregulation. In this case, after reaching the tumor

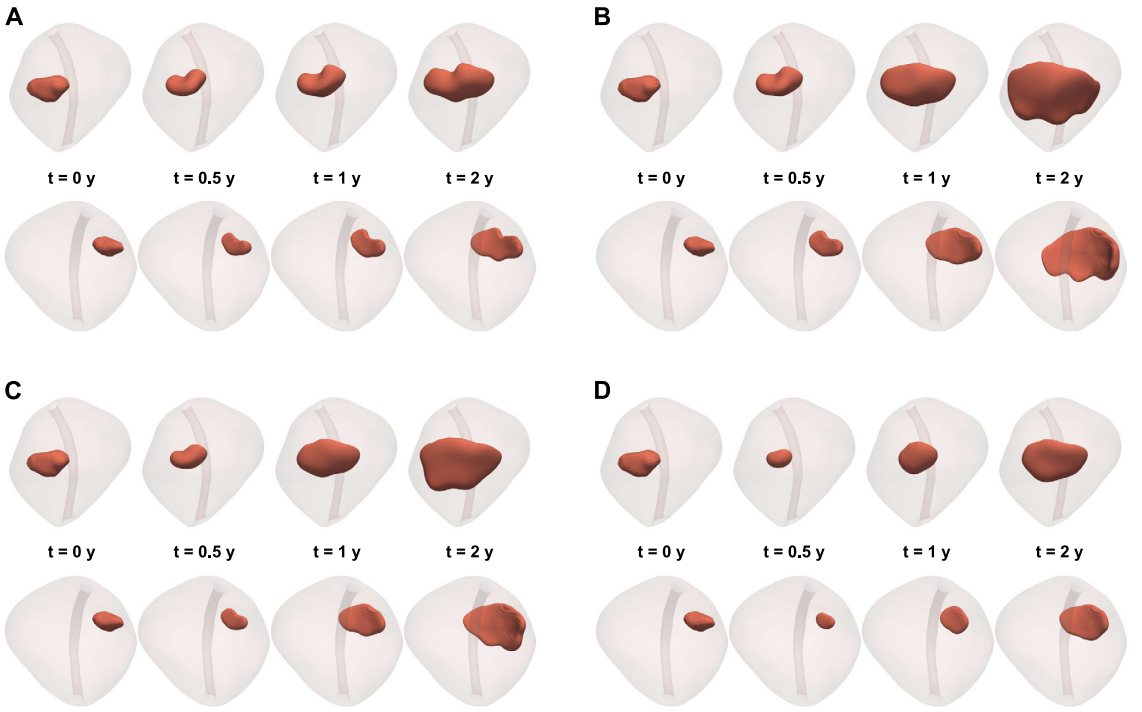

Fig. 5. Comparison of the mechanical and apoptotic effects of 5ARIs on the patient's tumor growth in different simulation scenarios using the strong prostate shrinkage law. (A) No intake of 5ARI (*in silico* control). (B) Mechanical effects only (unaltered apoptosis). (C) Mechanical effects combined with 5% upregulation of tumor apoptosis. (D) Mechanical effects combined with 10% upregulation of tumor apoptosis. The top and bottom rows in each subfigure show a posterior and anterior view of the prostate, respectively.

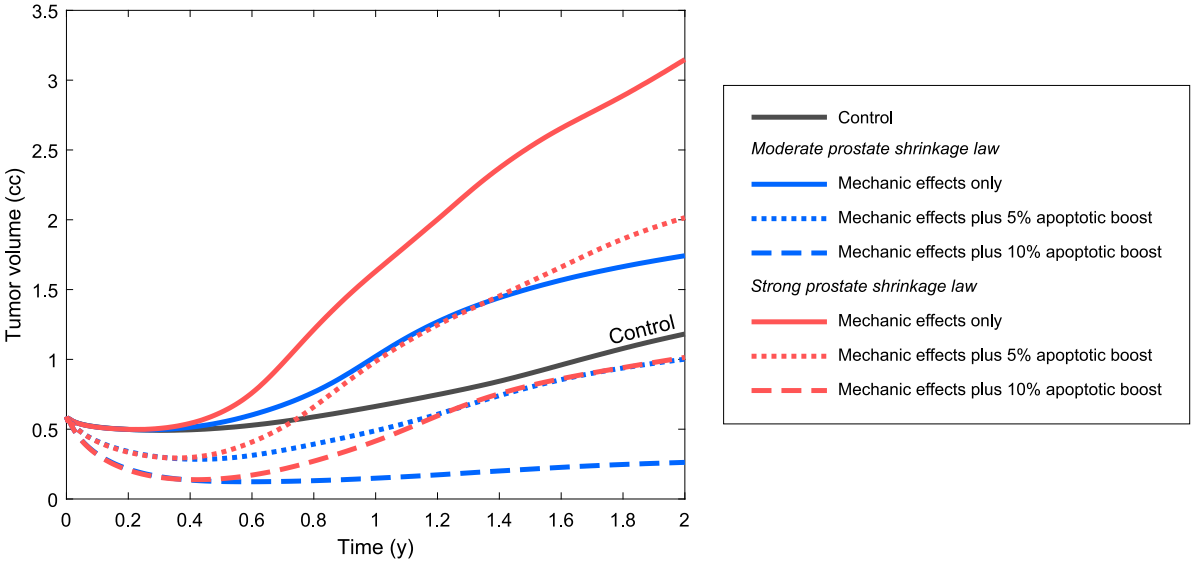

Fig. 6. Comparison plots of tumor volume evolution in the different simulation scenarios tested in this study.

volume minimum, PCa grew much slower than in the other simulations and always within the left superior PZ. Additionally, the final tumor volume was almost an order of magnitude smaller than the *in silico* control.

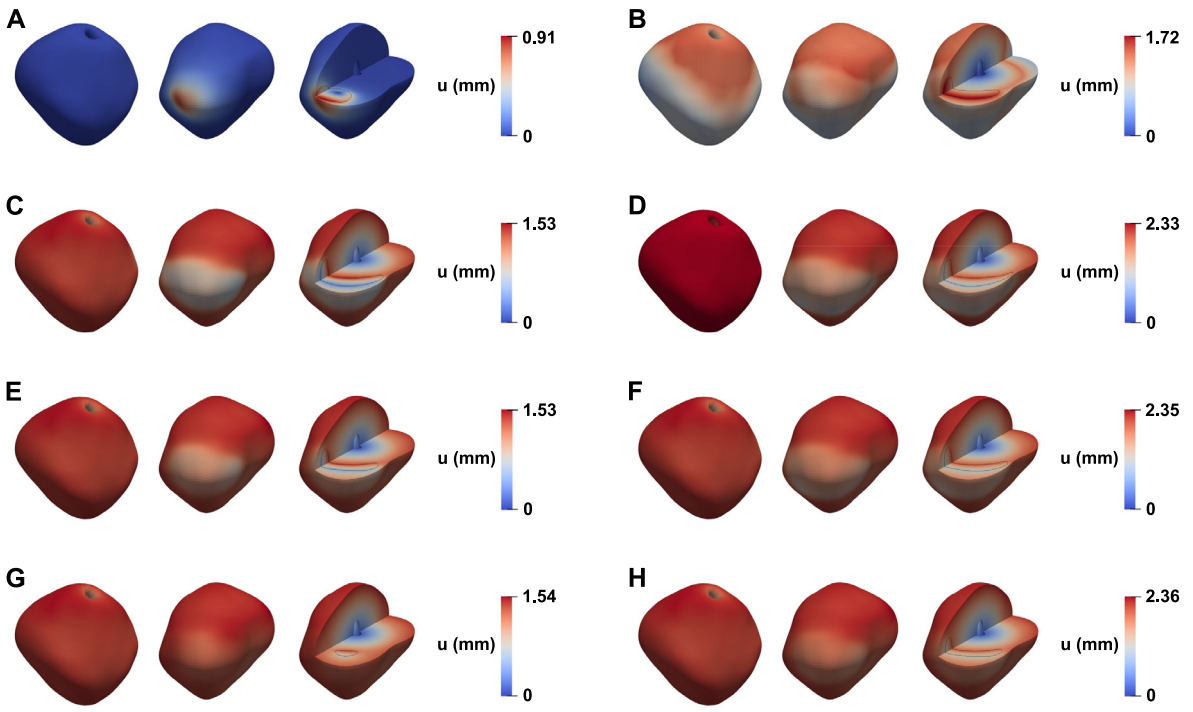

Fig. 7. Comparison of the deformation of the prostate in the different simulation scenarios of tumor growth tested in this study. Each subfigure represents the magnitude of the displacement field $\mathbf{u}_1$ over the whole prostate, from left to right: anterior view, posterior view, and section exposing the tumor region from posterior view. In the latter, the tumor is depicted with a black contour. (A) *In silico* control at $t = 0.02$ years, showing initial characteristic swelling deformation in all simulation scenarios. (B) *In silico* control at $t = 2$ years, showing the final deformation obtained in this simulation case. (C) Moderate prostate shrinkage law only at $t = 2$ years. (D) Strong prostate shrinkage law only at $t = 2$ years. (E) Moderate prostate shrinkage law plus mild apoptotic boost at $t = 2$ years. (F) Strong prostate shrinkage law plus mild apoptotic boost at $t = 2$ years. (G) Moderate prostate shrinkage law plus intense apoptotic boost at $t = 2$ years. (H) Strong prostate shrinkage law plus intense apoptotic boost at $t = 2$ years.

Fig. 7 shows a comparison of the deformation obtained in each simulation scenario in this study. The *in silico* control tumor generated a local swelling deformation and produced noticeable lumps on the left lateral and posterior external surface of the prostate, as shown in Fig. 7A–B. The CG expansion due to BPH progressively dominated the deformation (see Fig. 7B) and the tumor locally increased the displacement field $\mathbf{u}_1$ towards the outer part of the PZ, where the maximum magnitude of this displacement field was registered (1.16 mm at $t = 1$ year and 1.72 mm at $t = 2$ years). The 5ARI mechanical shrinkage imposed a displacement field $\mathbf{u}_1$ that compressed prostatic tissue inwards in a hydrostatic manner, as depicted in Figs. 3 and 7C–H. This deformation was predominant in all cases, except for a short time at the beginning of the simulations in which the tumor mass effect was more important than 5ARI shrinkage (approximately until $t = 0.25$ years with the moderate prostate shrinkage law and $t = 0.14$ years with the strong prostate shrinkage law). Hence, near the simulation onset, the displacement field $\mathbf{u}_1$ was directed outwards from the tumor and reached maximum values in the order of 0.7 to 0.8 mm on the tumor outer surface, much as in the *in silico* control in Fig. 7A. As 5ARI prostate shrinkage grew stronger, the displacement field $\mathbf{u}_1$ progressively became globally oriented towards the inner prostate. Thereafter, the tumor swelling deformation considerably reduced the magnitude of the displacement field $\mathbf{u}_1$ on its outer surface, while it slightly contributed to it on its inner surface, in contact with CG border (see Fig. 7C–H). This alteration of the displacement field $\mathbf{u}_1$ generated by 5ARI shrinkage became weaker as we increased the intensity of 5ARI apoptotic upregulation because the tumor consequently grew smaller and more slowly, hence creating smaller displacements. For instance, at $t = 2$ years the minimum magnitude of the displacement field $\mathbf{u}_1$ on the tumor outer surface with the moderate prostate shrinkage law plus no, mild, or intense apoptotic boost was 0.35 mm, 0.54 mm, and 0.78 mm, respectively; whereas the maximum magnitude of the displacement field $\mathbf{u}_1$ on the tumor inner surface was respectively 1.43 mm,

1.37 mm, and 1.32 mm. For the combination of the strong prostate shrinkage with no, mild, or intense upregulation of tumor apoptosis, the corresponding minima on the outer tumor surface at $t = 2$ years were respectively 0.87 mm, 0.98 mm, and 1.14 mm; whereas the maxima on the inner tumor surface were 2.04 mm, 2.00 mm, and 1.97 mm, respectively. Once 5ARI shrinkage dominated the prostate deformation, the magnitude of displacement field $\mathbf{u}_1$ on the prostate surface was smaller close to the tumor region. Far from such area, the magnitude of the displacement vector $\mathbf{u}_1$ reached its maximum value, much as in Section 5.2, and did not vary meaningfully when we introduced either apoptotic boost. At $t = 2$ years, this maximum value was around 1.5 mm with the moderate prostate shrinkage law and approximately 2.4 mm with the strong prostate shrinkage law (see Fig. 7C–H).

In the *in silico* control simulation, the enlargement of the CG due to BPH produced a total stress field $\boldsymbol{\sigma} = \boldsymbol{\sigma}_0 + \boldsymbol{\sigma}_1$ characterized by high Von Mises stress within the PZ, which peaked on the CG border (2.7 to 4.2 KPa at $t = 2$ years) and decreased towards the external surface of the prostate (1.0 to 2.7 KPa at $t = 2$ years). The Von Mises stress was also high on the external surface of the tumor (1.7 to 2.7 KPa at $t = 2$ years) and accumulated along the urethra (3 to 8 KPa). Within the CG, the Von Mises stress was much lower (0.1 to 1.8 KPa at $t = 2$ years) but the hydrostatic stress peaked at compressive values (-3.1 to -2.6 KPa at $t = 2$ years) and also accumulated along the urethra (-4.5 to -3 KPa at $t = 2$ years). In the PZ, the hydrostatic component of the total stress $\boldsymbol{\sigma} = \boldsymbol{\sigma}_0 + \boldsymbol{\sigma}_1$ was also compressive but lower than in the CG (-0.7 to -0.1 KPa at $t = 2$ years), except within the tumor, where it was slightly more intense (-1.0 to -0.7 KPa at $t = 2$ years). In the simulations including 5ARI treatment, the total stress field $\boldsymbol{\sigma} = \boldsymbol{\sigma}_0 + \boldsymbol{\sigma}_1$ was mostly characterized by the prostate shrinkage deformation, as outlined in Section 5.2. As in the *in silico* control simulation, PCa locally increased the Von Mises stress around the external surface of the tumor (reaching approximately 1.5 to 2.5 KPa at $t = 2$ years) and contributed to a compressive hydrostatic state in its inside (-0.7 to -0.4 KPa with the moderate prostate shrinkage law and -0.5 to -0.2 with the strong prostate shrinkage law at $t = 2$ years).

6. Discussion

In this work, we propose that the outcome of 5ARI therapy to inhibit PCa growth depends on the combined action of mechanical stress release due to prostate shrinkage and the upregulation of apoptosis. By including these effects of 5ARIs in our previous organ-scale, mechanically-coupled model of PCa growth [69], we ran a simulation study to explore this hypothesis and gain insight into the controversial effects of 5ARIs on aggressive tumors. Our results show that the shrinkage of the prostate induced by 5ARIs reduced the hydrostatic stress that had accumulated over years of BPH in prostatic tissue, which led to a mechanical state that favored the development of PCa. In this situation, tumors grew at a faster pace, showing higher invasiveness, and reaching larger volumes, which are more likely to evolve towards advanced, potentially lethal disease [1,69,121,122]. Our simulations also show that a concomitant upregulation of apoptosis by 5ARIs counteracted this mechanism. However, this apoptotic boost could only effectively delay PCa growth with respect to the *in silico* control case if it was sufficiently intense to overcome the mechanical stress release derived from prostate shrinkage. This happened in all cases involving the moderate prostate shrinkage law and when a strong prostate volumetric reduction was accompanied by an intense upregulation of apoptosis.

5ARI pro-apoptotic effects dominated PCa dynamics during the first months of treatment regardless of the prostate shrinkage law used in the simulation (see Figs. 4–6). This resulted in an initial volumetric decrease of the tumor in all simulation scenarios accounting for apoptotic upregulation. The reduction in tumor volume observed in this study aligns with recent results from a short-term study of secondary chemoprevention using dutasteride in which tumor volumes were measured with MR imaging [123]. However, an initial decrease in tumor volume did not directly indicate a successful outcome of 5ARI treatment in the simulations of this study. The tumor-promoting effects derived from the release of mechanical stress became stronger later, as the prostate shrinkage approximated its asymptotic value. Hence, long-term PCa dynamics was governed by the combination of this mechanical effect and apoptotic upregulation. Thus, our results suggest that patients should be closely followed as long as they use 5ARIs, and might require further clinical action should a trend towards fast dynamics and larger volume be detected.

The magnitude of the displacement field on the prostate surface close to the tumor was noticeably smaller (see Fig. 7), which would facilitate the detection of the tumor with digital rectal examination during regular patient follow-up. The PCa growth morphologies observed in this study would also enable the detection of tumors with standard biopsies. However, a biopsy needle entering the prostate from the posterior aspect of the PZ could laterally hit the cancerous mass or simply probe one of the extremes of the curved tumor, which would underestimate the

patient's tumor burden (see Figs. 4 and 5). According to our simulations, a tumor may also take years to show up in a biopsy sample from a region of the prostate adjacent to the origin site (see Figs. 4 and 5), but it may have considerably grown and evolved to a more advanced case of PCa by then. Alternatively, MR-guided biopsies and multiparametric MR imaging would permit a closer control on tumor growth morphology and evolution, facilitating the detection of large tumor volumes, rapid dynamics, and an invasive demeanor.

Tumor dynamics and phenotypes do not only vary from patient to patient, but also as the tumor evolves towards a more advanced stage [1,13,14,54,58]. Patients whose tumor is less dependent on the androgen signaling pathways regulated by 5α-reductase enzymes may exhibit a poorer upregulation of tumor apoptosis during 5ARI therapy and hence experience a worse control of PCa growth. This might have been the case for the advanced tumors detected among 5ARI users in PCPT and REDUCE trials [35–37]. Additionally, this mechanism would also explain the variability in tumor delay among PCa patients taking 5ARIs in secondary chemoprevention studies [45–51]. Therefore, our results call for a better characterization of the pivotal role of apoptotic upregulation during 5ARI therapy for PCa by quantifying this phenomenon over time and in different stages of the disease [14,54,58].

The work presented herein presents some limitations to be addressed in future studies. The anatomic model of the patient's prostate can be enriched in different ways, for instance: segmenting the BPH nodules and imposing the pressure load associated with this pathology over their volume; accounting for different histopathological tissue architectures within the tumor, which correspond to different stages of the disease and may show different dynamics and response to 5ARIs [14,54,58]; introducing a heterogeneous parameterization of the mechanical properties and apoptotic upregulation of the different intraprostatic regions, which may vary depending on the relative proportion of epithelial and stromal tissue [1,5,22–27,94–99]; and defining spatially varying Winkler-inspired boundary conditions on the external surface of the prostate to model how the different tissues and organs surrounding the prostate mechanically react to the deformation of this organ. Indeed, improving our understanding on these mechanical boundary conditions would contribute to gain a great insight on the mechanical inhibition of PCa growth and the mechanical action of 5ARIs described herein because these boundary conditions play a central role in the accumulation of hydrostatic stress in the prostate. The upregulation of tumor apoptosis was assumed to be constant in time in this study, but some studies suggest that it may have more complex dynamics [22,23,25,26,52–57]. Precise and extensive quantification of apoptosis over time would be necessary to improve the modeling of this phenomenon. Future research could also explore more advanced models of the BPH load [101–103] as well as tumor growth and deformation [60,79–81,90,91,93]. Additionally, the influence of mechanical stress on tumor dynamics could be refined by defining various mechanotransductive functions affecting tumor mobility, proliferation and apoptosis independently [59–61,80,81]. Testing alternative mathematical definitions for these mechanotransductive functions would also contribute to better understand the mechanical inhibition of tumor growth. Moreover, 5ARIs have been suggested to improve the accuracy of PSA as a PCa biomarker by reducing the contribution to PSA by BPH tissue and better exposing any PSA produced by tumors [13,21,38,43,44]. The computational model used in this study could be extended to include an equation for PSA dynamics as in [69,73], but this would require previously quantifying how 5ARI therapy alters PSA dynamics due to the reduction of DHT levels [13,19,21].

Additionally, we acknowledge that the strain values may happen to be somewhat outside the admissible range for linear elasticity in a few localized regions along the tumor interface. Furthermore, $\boldsymbol{\sigma}^0$ is just a rough estimate of the stress state induced by BPH prior to PCa detection at the MR date. However, we are only interested in obtaining an acceptable estimation of the mechanical stress fields in the prostate to compute the mechanotransductive factor $M(\boldsymbol{\sigma})$ and hence adjust tumor dynamics in Eq. (1). This study also features other major sources of uncertainty beyond linear elasticity, such as prostate and tumor segmentation, the PCa model itself, and the mechanical boundary conditions. Still, in [69] we observed that our mechanically-coupled model qualitatively reproduced the inhibiting effect of the tumor mass effect and BPH on PCa growth. To verify the validity of the use of linear kinematic theory, we computed the symmetrical and skew-symmetrical components of the displacement gradient with respect to the initial configuration, and determined that they were sufficiently small that their products were not substantial compared with the linear terms. We also observed that the skew-symmetric components were negligible everywhere. Consequently, we feel confident that the simulation results presented in Section 5 provide physically meaningful information. In the future, we plan to investigate formulations accounting for geometric and material nonlinearities as well as alternative constitutive equations for the prostate tissue to improve the accuracy of the computed displacement and stress fields [64,65,89,124,125]. Additionally, a poroelastic model could be explored to analyze the effect of mechanical deformation on nutrient transport and distribution [60], which would enable the study of the heterogeneous intratumoral metabolism and drug delivery.

Finally, the mechanism of 5ARI action on PCa growth proposed in this study needs to be assessed using personalized longitudinal data within a patient cohort. If validated, this mechanism could shed light into the controversial debate around the use of 5ARIs for chemoprevention of PCa, which is arguably one of the major issues currently in the clinical management of PCa. The computational technology used in this study can offer a unique approach to monitor patients using 5ARIs, the early identification of responders and non-responders, and improve our understanding of the effects of these drugs on tumor dynamics. Patient-specific longitudinal clinical and imaging data can be used to parameterize our mathematical model of PCa growth. Multiparametric MR imaging is increasingly being used in the clinical management of PCa and has the potential to provide a wealth of information, including both tumor and prostate geometry as well as PCa architecture and aggressiveness [126]. A sensitivity analysis can inform on which parameters have the highest impact on model results and hence should be calibrated from patient's data, while the remainder could be fixed based on prior clinical studies. A model calibration study may also provide information about the potential benefits of defining spatially-varying parameter maps versus global values. Finally, inverse or machine learning methods could be used to extract personalized parameter values based on each patient's longitudinal dataset. Then, predictive simulations would enable physicians to assess the efficacy of 5ARI therapy and anticipate pathological complications. Moreover, these simulations would assist physicians to define a personalized monitoring strategy by determining the best time to obtain new medical images and perform clinical tests. Predicted tumor growth could also be used to guide further biopsies [69,73]. By using this approach on a cohort of PCa patients, it would also be possible to explore the pro-apoptotic effect of 5ARIs by analyzing the distribution of the parameter A in Eq. (1). Additionally, our computational model could serve as a powerful and versatile means to explore innovative approaches to delay PCa growth overcoming the tumor-promoting mechanical stress release associated to 5ARI-induced prostate shrinkage.

Acknowledgments

G.L. and A.R. were partially supported by the MIUR-PRIN project XFAST-SIMS (no. 20173C478N). The authors acknowledge the Rosen Center for Advanced Computing at Purdue University (USA) for providing HPC resources that contributed to the results presented in this paper.

Appendix A. Supplementary data

Supplementary material related to this article can be found online at https://doi.org/10.1016/j.cma.2020.112843.

References

[1] A.J. Wein, L.R. Kavoussi, A.C. Novick, A.W. Partin, C.A. Peters, Campbell-Walsh Urology: Expert Consult Premium Edition: Enhanced Online Features and Print, 4-Volume Set, tenth ed., Elsevier Saunders, 2012.
[2] S.J. Berry, D.S. Coffey, P.C. Walsh, L.L. Ewing, The development of human benign prostatic hyperplasia with age, J. Urol. 132 (3) (1984) 474–479.
[3] B. Chughtai, J.C. Forde, D.D.M. Thomas, L. Laor, T. Hossack, H.H. Woo, A.E. Te, S.A. Kaplan, Benign prostatic hyperplasia, Nature Rev. Dis. Primers 2 (2016) 16031.
[4] F.V. Coakley, H. Hricak, Radiologic anatomy of prostate gland: a clinical approach, Radiol. Clin. North Am. 38 (1) (2000) 15–30.
[5] G.M. Villeirs, K. L.Verstraete, W.J.D. Neve, G.O.D. Meerleer, Magnetic resonance imaging anatomy of prostate and periprostatic area: a guide for radiotherapists, Radiother. Oncol. 76 (1) (2005) 99–106.
[6] V. Mirone, F. Fusco, P. Verze, C. Schulman, F. Debruyne, C. Imbimbo, Androgens and benign prostatic hyperplasia, Eur. Urol. Suppl. 5 (4) (2006) 410–417.
[7] C. Carson, R. Rittmaster, The role of dihydrotestosterone in benign prostatic hyperplasia, Urology 61 (4, Suppl. 1) (2003) 2–7.
[8] F. Bray, J. Ferlay, I. Soerjomataram, R.L. Siegel, L.A. Torre, A. Jemal, Global cancer statistics 2018: GLOBOCAN estimates of incidence and mortality worldwide for 36 cancers in 185 countries, CA Cancer J. Clin. 68 (6) (2018) 394–424.
[9] A. Erbersdobler, H. Augustin, T. Schlomm, R.-P. Henke, Prostate cancers in the transition zone: Part 1; pathological aspects, BJU Int. 94 (9) (2004) 1221–1225.
[10] C. Buzzoni, A. Auvinen, M.J. Roobol, S. Carlsson, S.M. Moss, D. Puliti, H.J. de Koning, C.H. Bangma, L.J. Denis, M. Kwiatkowski, et al., Metastatic prostate cancer incidence and prostate-specific antigen testing: new insights from the European randomized study of screening for prostate cancer, Eur. Urol. 68 (5) (2015) 885–890.
[11] A. Godoy, E. Kawinski, Y. Li, D. Oka, B. Alexiev, F. Azzouni, M.A. Titus, J.L. Mohler, 5α-reductase type 3 expression in human benign and malignant tissues: A comparative analysis during prostate cancer progression, Prostate 71 (10) (2011) 1033–1046.
[12] D.J. Tindall, R.S. Rittmaster, The rationale for inhibiting 5α-reductase isoenzymes in the prevention and treatment of prostate cancer, J. Urol. 179 (4) (2008) 1235–1242.

[13] L.P. Nacusi, D.J. Tindall, Targeting 5α-reductase for prostate cancer prevention and treatment, Nature Reviews Urology 8 (2011) 378–384.
[14] C.J. Logothetis, G.E. Gallick, S.N. Maity, J. Kim, A. Aparicio, E. Efstathiou, S.-H. Lin, Molecular classification of prostate cancer progression: Foundation for marker-driven treatment of prostate cancer, Cancer Discov. 3 (8) (2013) 849–861.
[15] F. Habib, M. Ross, C. Bayne, K. Grigor, A. Buck, P. Bollina, K. Chapman, The localisation and expression of 5 alpha-reductase types I and II mRNAs in human hyperplastic prostate and in prostate primary cultures, J. Endocrinol. 156 (3) (1998) 509–517.
[16] C. Iehlé, F. cois Radvanyi, S.G.D. de Medina, L. Ouafik, H. Gérard, D. Chopin, J.-P. Raynaud, P.-M. Martin, Differences in steroid 5α-reductase iso-enzymes expression between normal and pathological human prostate tissue, J. Steroid. Biochem. Mol. Biol. 68 (5) (1999) 189–195.
[17] L.N. Thomas, C. Lazier, R. Gupta, R. Norman, D. Troyer, S. O'Brien, R. Rittmaster, Differential alterations in 5α-reductase type 1 and type 2 levels during development and progression of prostate cancer, Prostate 63 (3) (2005) 231–239.
[18] L.N. Thomas, R.C. Douglas, C.B. Lazier, R. Gupta, R.W. Norman, P.R. Murphy, R.S. Rittmaster, C.K. Too, Levels of 5α-reductase type 1 and type 2 are increased in localized high grade compared to low grade prostate cancer, J. Urol. 179 (1) (2008) 147–151.
[19] F. Azzouni, J. Mohler, Role of 5α-reductase inhibitors in benign prostatic diseases, Prostate Cancer Prostatic Dis. 15 (3) (2012) 222.
[20] M. Oelke, A. Bachmann, A. Descazeaud, M. Emberton, S. Gravas, M.C. Michel, J. N'Dow, J. Nordling, J.J. de la Rosette, EAU guidelines on the treatment and follow-up of non-neurogenic male lower urinary tract symptoms including benign prostatic obstruction, Eur. Urol. 64 (1) (2013) 118–140.
[21] F. Azzouni, J. Mohler, Role of 5α-reductase inhibitors in prostate cancer prevention and treatment, Urology 79 (6) (2012) 1197–1205.
[22] R.S. Rittmaster, R.W. Norman, L.N. Thomas, G. Rowden, Evidence for atrophy and apoptosis in prostates of men given finasteride, J. Clin. Endocrinol. Metab. 81 (2) (1996) 814–819.
[23] D.T. Glassman, J.K. Chon, A. Borkowski, S.C. Jacobs, N. Kyprianou, Combined effect of terazosin and finasteride on apoptosis, cell proliferation, and transforming growth factor-β expression in benign prostatic hyperplasia, Prostate 46 (1) (2001) 45–51.
[24] L.S. Marks, A.W. Partin, F.J. Dorey, G.J. Gormley, J.I. Epstein, J.B. Garris, M.L. Macairan, E.D. Shery, P.B. Santos, E. Stoner, et al., Long-term effects of finasteride on prostate tissue composition, Urology 53 (3) (1999) 574–580.
[25] C. Lazier, L. Thomas, R. Douglas, J. Vessey, R. Rittmaster, Dutasteride, the dual 5α–reductase inhibitor, inhibits androgen action and promotes cell death in the LNCaP prostate cancer cell line, Prostate 58 (2) (2004) 130–144.
[26] A. Tsujimura, S. Fukuhara, T. Soda, K. Takezawa, H. Kiuchi, T. Takao, Y. Miyagawa, N. Nonomura, S. Adachi, Y. Tokita, T. Nomura, Histologic evaluation of human benign prostatic hyperplasia treated by dutasteride: A study by xenograft model with improved severe combined immunodeficient mice, Urology 85 (1) (2015) 274.e1 – 274.e8.
[27] K.A. Iczkowski, J. Qiu, J. Qian, M.C. Somerville, R.S. Rittmaster, G.L. Andriole, D.G. Bostwick, The dual 5-alpha-reductase inhibitor dutasteride induces atrophic changes and decreases relative cancer volume in human prostate, Urology 65 (1) (2005) 76–82.
[28] L.S. Marks, C.G. Roehrborn, E. Wolford, T.H. Wilson, The effect of dutasteride on the peripheral and transition zones of the prostate and the value of the transition zone index in predicting treatment response, J. Urol. 177 (4) (2007) 1408–1413.
[29] J.D. McConnell, R. Bruskewitz, P. Walsh, G. Andriole, M. Lieber, H.L. Holtgrewe, P. Albertsen, C.G. Roehrborn, J.C. Nickel, D.Z. Wang, A.M. Taylor, J. Waldstreicher, The effect of finasteride on the risk of acute urinary retention and the need for surgical treatment among men with benign prostatic hyperplasia, New Engl. J. Med. 338 (9) (1998) 557–563.
[30] F.C. Lowe, J.D. McConnell, P.B. Hudson, N.A. Romas, R. Boake, M. Lieber, M. Elhilali, J. Geller, J. Imperto-McGinely, G.L. Andriole, R.C. Bruskewitz, P.C. Walsh, G. Bartsch, J.N. Nacey, S. Shah, F. Pappas, A. Ko, T. Cook, E. Stoner, J. Waldstreicher, Long-term 6-year experience with finasteride in patients with benign prostatic hyperplasia, Urology 61 (4) (2003) 791–796.
[31] F. Debruyne, J. Barkin, P. van Erps, M. Reis, T.L.J. Tammela, C. Roehrborn, Efficacy and safety of long-term treatment with the dual 5α-reductase inhibitor dutasteride in men with symptomatic benign prostatic hyperplasia, Eur. Urol. 46 (4) (2004) 488–495.
[32] S.A. Kaplan, C.G. Roehrborn, J.D. McConnell, A.G. Meehan, S. Surynawanshi, J.Y. Lee, J. Rotonda, J.W. Kusek, L.M. Nyberg Jr., M.T. of Prostatic Symptoms Research Group, et al., Long-term treatment with finasteride results in a clinically significant reduction in total prostate volume compared to placebo over the full range of baseline prostate sizes in men enrolled in the MTOPS trial, J. Urol. 180 (3) (2008) 1030–1033.
[33] R.V. Clark, D.J. Hermann, G.R. Cunningham, T.H. Wilson, B.B. Morrill, S. Hobbs, Marked suppression of dihydrotestosterone in men with benign prostatic hyperplasia by dutasteride, a dual 5α-reductase inhibitor, J. Clin. Endocrinol. Metab. 89 (5) (2004) 2179–2184.
[34] J.C. Nickel, P. Gilling, T.L. Tammela, B. Morrill, T.H. Wilson, R.S. Rittmaster, Comparison of dutasteride and finasteride for treating benign prostatic hyperplasia: the enlarged prostate international comparator study (EPICS), BJU Int. 108 (3) (2011) 388–394.
[35] I.M. Thompson, P.J. Goodman, C.M. Tangen, M.S. Lucia, G.J. Miller, L.G. Ford, M.M. Lieber, R.D. Cespedes, J.N. Atkins, S.M. Lippman, S.M. Carlin, A. Ryan, C.M. Szczepanek, J.J. Crowley, C.A.J. Coltman, The influence of finasteride on the development of prostate cancer, New Engl. J. Med. 349 (3) (2003) 215–224.
[36] I.M. Thompson, P.J. Goodman, C.M. Tangen, H.L. Parnes, L.M. Minasian, P.A. Godley, M.S. Lucia, L.G. Ford, Long-term survival of participants in the prostate cancer prevention trial, New Engl. J. Med. 369 (7) (2013) 603–610, PMID: 23944298.
[37] G.L. Andriole, D.G. Bostwick, O.W. Brawley, L.G. Gomella, M. Marberger, F. Montorsi, C.A. Pettaway, T.L. Tammela, C. Teloken, D.J. Tindall, M.C. Somerville, T.H. Wilson, I.L. Fowler, R.S. Rittmaster, Effect of dutasteride on the risk of prostate cancer, New Engl. J. Med. 362 (13) (2010) 1192–1202.
[38] M.A. Liss, I.M. Thompson, Prostate cancer prevention with 5-alpha reductase inhibitors: concepts and controversies, Curr. Opin. Urol. 28 (1) (2018) 42–45.
[39] M.R. Theoret, Y.-M. Ning, J.J. Zhang, R. Justice, P. Keegan, R. Pazdur, The risks and benefits of 5α-reductase inhibitors for prostate-cancer prevention, New Engl. J. Med. 365 (2) (2011) 97–99.
[40] M.S. Lucia, J.I. Epstein, P.J. Goodman, A.K. Darke, V.E. Reuter, F. Civantos, C.M. Tangen, H.L. Parnes, S.M. Lippman, F.G. La Rosa, et al., Finasteride and high-grade prostate cancer in prostate cancer prevention trial, J. Natl. Cancer Inst. 99 (18) (2007) 1375–1383.

[41] T. Murtola, T. Tammela, L. Määttänen, M. Ala-opas, U. Stenman, A. Auvinen, Prostate cancer incidence among finasteride and alpha-blocker users in the finnish prostate cancer screening trial, Br. J. Cancer 101 (2009) 843–848.
[42] M.A. Preston, K.M. Wilson, S.C. Markt, R. Ge, C. Morash, M.J. Stampfer, M. Loda, E. Giovannucci, L.A. Mucci, A.F. Olumi, 5α-reductase inhibitors and risk of high-grade or lethal prostate cancer, JAMA Intern. Med. 174 (8) (2014) 1301–1307.
[43] R. Serfling, M. Shulman, G. Thompson, Z. Xiao, E. Benaim, C.G. Roehrborn, R. Rittmaster, Quantifying the impact of prostate volumes, number of biopsy cores and 5α-reductase inhibitor therapy on the probability of prostate cancer detection using mathematical modeling, J. Urol. 177 (6) (2007) 2352–2356.
[44] M.W. Redman, C.M. Tangen, P.J. Goodman, M.S. Lucia, C.A. Coltman, I.M. Thompson, Finasteride does not increase the risk of high-grade prostate cancer: A bias-adjusted modeling approach, Cancer Prev. Res. 1 (3) (2008) 174–181.
[45] P.Q. Shelton, A.N. Ivanowicz, C.M. Wakeman, M.G. Rydberg, J. Norton, S.B. Riggs, C.M. Teigland, Active surveillance of very-low-risk prostate cancer in the setting of active treatment of benign prostatic hyperplasia with 5α-reductase inhibitors, Urology 81 (5) (2013) 979–985.
[46] A. Finelli, G. Trottier, N. Lawrentschuk, R. Sowerby, A.R. Zlotta, L. Radomski, N. Timilshina, A. Evans, T.H. van der Kwast, A. Toi, M.A. Jewett, J. Trachtenberg, N.E. Fleshner, Impact of 5α-reductase inhibitors on men followed by active surveillance for prostate cancer, Eur. Urol. 59 (4) (2011) 509–514.
[47] P.O. Richard, A. Finelli, 5-alpha reductase inhibitors in active surveillance, Curr. Opin. Urol. 24 (3) (2014) 324–328.
[48] N.E. Fleshner, M.S. Lucia, B. Egerdie, L. Aaron, G. Eure, I. Nandy, L. Black, R.S. Rittmaster, Dutasteride in localised prostate cancer management: the REDEEM randomised, double-blind, placebo-controlled trial, Lancet 379 (9821) (2012) 1103–1111.
[49] D. Margel, I. Nandy, T.H. Wilson, R. Castro, N. Fleshner, Predictors of pathological progression among men with localized prostate cancer undergoing active surveillance: a sub-analysis of the REDEEM study, J. Urol. 190 (6) (2013) 2039–2046.
[50] A.E. Ross, Z. Feng, P.M. Pierorazio, P. Landis, P.C. Walsh, H.B. Carter, B.J. Trock, E.M. Schaeffer, Effect of treatment with 5-α reductase inhibitors on progression in monitored men with favourable-risk prostate cancer, BJU Int. 110 (5) (2012) 651–657.
[51] C. Dai, V. Ganesan, J. Zabell, Y.A. Nyame, N. Almassi, D.J. Greene, D. Hettel, C. Reichard, S.C. Haywood, H. Arora, A. Zampini, A. Crane, J. Li, A. Elshafei, C. Magi-Galluzzi, R.J. Stein, K. Fareed, M. Gong, J.S. Jones, E.A. Klein, A.J. Stephenson, Impact of 5α-reductase inhibitors on disease reclassification among men on active surveillance for localized prostate cancer with favorable features, J. Urol. 199 (2) (2018) 445–452.
[52] C. Festuccia, G.L. Gravina, P. Muzi, R. Pomante, A. Angelucci, C. Vicentini, M. Bologna, Effects of dutasteride on prostate carcinoma primary cultures: A comparative study with finasteride and MK386, J. Urol. 180 (1) (2008) 367–372.
[53] G. Andriole, P. Humphrey, P. Ray, M. Gleave, J. Trachtenberg, L. Thomas, C. Lazier, R. Rittmaster, Effect of the dual 5α-reductase inhibitor dutasteride on markers of tumor regression in prostate cancer, J. Urol. 172 (3) (2004) 915–919.
[54] J. Kim, J.W. Davis, E.A. Klein, C. Magi-Galluzzi, Y. Lotan, J.F. Ward, L.L. Pisters, J.W. Basler, C.A. Pettaway, A. Stephenson, E.M.L.N. Tapia, E. Efstathiou, X. Wang, K.-A. Do, J.J. Lee, I.P. Gorlov, L.A. Vornik, A.M. Hoque, I.N. Prokhorova, H.L. Parnes, S.M. Lippman, I.M. Thompson, P.H. Brown, C.J. Logothetis, P. Troncoso, Tissue effects in a randomized controlled trial of short-term finasteride in early prostate cancer, EBioMedicine 7 (2016) 85–93.
[55] A.M. McCrohan, C. Morrissey, C. O'Keane, N. Mulligan, C. Watson, J. Smith, J.M. Fitzpatrick, R.W.G. Watson, Effects of the dual 5 primary cultures of prostate cancer epithelial cells and cell lines, Cancer 106 (12) (2006) 2743–2752.
[56] R. Bass, B. Perry, P. Langenstroer, J.B. Thrasher, K.L. Dennis, O. Tawfik, J. Holzbeierlein, Effects of short-term finasteride on apoptotic factors and androgen receptors in prostate cancer cells, J. Urol. 181 (2) (2009) 615–620.
[57] M. Gleave, J. Qian, C. Andreou, P. Pommerville, J. Chin, R. Casey, G. Steinhoff, N. Fleshner, D. Bostwick, L. Thomas, R. Rittmaster, on behalf of the ARI40010 Study Team, The effects of the dual 5α-reductase inhibitor dutasteride on localized prostate cancer—results from a 4-month pre-radical prostatectomy study, Prostate 66 (15) (2006) 1674–1685.
[58] J. Li, J. Kim, Molecular profiles of finasteride effects on prostate carcinogenesis, Cancer Prev. Res. 2 (6) (2009) 518–524.
[59] G. Helmlinger, P.A. Netti, H.C. Lichtenbeld, R.J. Melder, R.K. Jain, Solid stress inhibits the growth of multicellular tumor spheroids, Nature Biotechnol. 15 (8) (1997) 778–783.
[60] T. Roose, P.A. Netti, L.L. Munn, Y. Boucher, R.K. Jain, Solid stress generated by spheroid growth estimated using a linear poroelasticity model, Microvasc. Res. 66 (3) (2003) 204–212.
[61] G. Cheng, J. Tse, R.K. Jain, L.L. Munn, Micro-environmental mechanical stress controls tumor spheroid size and morphology by suppressing proliferation and inducing apoptosis in cancer cells, PLoS One 4 (2) (2009) 1–11.
[62] T. Stylianopoulos, J.D. Martin, M. Snuderl, F. Mpekris, S.R. Jain, R.K. Jain, Coevolution of solid stress and interstitial fluid pressure in tumors during progression: Implications for vascular collapse, Cancer Res. 73 (13) (2013) 3833–3841.
[63] R.K. Jain, J.D. Martin, T. Stylianopoulos, The role of mechanical forces in tumor growth and therapy, Annu. Rev. Biomed. Eng. 16 (1) (2014) 321–346.
[64] C. Voutouri, F. Mpekris, P. Papageorgis, A.D. Odysseos, T. Stylianopoulos, Role of constitutive behavior and tumor-host mechanical interactions in the state of stress and growth of solid tumors, PLoS One 9 (8) (2014) 1–9.
[65] M. Fraldi, A.R. Carotenuto, Cells competition in tumor growth poroelasticity, J. Mech. Phys. Solids 112 (2018) 345–367.
[66] S.J. Freedland, W.B. Isaacs, E.A. Platz, M.K. Terris, W.J. Aronson, C.L. Amling, J.C. Presti Jr., C.J. Kane, Prostate size and risk of high-grade, advanced prostate cancer and biochemical progression after radical prostatectomy: a search database study, J. Clin. Oncol. 23 (30) (2005) 7546–7554.
[67] W. Kassouf, H. Nakanishi, A. Ochiai, K.N. Babaian, P. Troncoso, R.J. Babaian, Effect of prostate volume on tumor grade in patients undergoing radical prostatectomy in the era of extended prostatic biopsies, J. Urol. 178 (1) (2007) 111–114.
[68] A. Briganti, F.K.-H. Chun, N. Suardi, A. Gallina, J. Walz, M. Graefen, S. Shariat, A. Ebersdobler, P. Rigatti, P. Perrotte, et al., Prostate volume and adverse prostate cancer features: fact not artifact, Eur. J. Cancer 43 (18) (2007) 2669–2677.

[69] G. Lorenzo, T.J.R. Hughes, P. Dominguez-Frojan, A. Reali, H. Gomez, Computer simulations suggest that prostate enlargement due to benign prostatic hyperplasia mechanically impedes prostate cancer growth, Proc. Natl. Acad. Sci. 116 (4) (2019) 1152–1161.
[70] A.R. Anderson, V. Quaranta, Integrative mathematical oncology, Nature Rev. Cancer 8 (3) (2008) 227–234.
[71] T.E. Yankeelov, N. Atuegwu, D. Hormuth, J.A. Weis, S.L. Barnes, M.I. Miga, E.C. Rericha, V. Quaranta, Clinically relevant modeling of tumor growth and treatment response, Sci. Transl. Med. 5 (187) (2013) 187ps9.
[72] J.T. Oden, E.A.B.F. Lima, R.C. Almeida, Y. Feng, M.N. Rylander, D. Fuentes, D. Faghihi, M.M. Rahman, M. DeWitt, M. Gadde, J.C. Zhou, Toward predictive multiscale modeling of vascular tumor growth, Arch. Comput. Methods Eng. 23 (4) (2016) 735–779.
[73] G. Lorenzo, M.A. Scott, K. Tew, T.J.R. Hughes, Y.J. Zhang, L. Liu, G. Vilanova, H. Gomez, Tissue-scale, personalized modeling and simulation of prostate cancer growth, Proc. Natl. Acad. Sci. 113 (48) (2016) E7663–E7671.
[74] C.H. Wang, J.K. Rockhill, M. Mrugala, D.L. Peacock, A. Lai, K. Jusenius, J.M. Wardlaw, T. Cloughesy, A.M. Spence, R. Rockne, E.C. Alvord, K.R. Swanson, Prognostic significance of growth kinetics in newly diagnosed glioblastomas revealed by combining serial imaging with a novel biomathematical model, Cancer Res. 69 (23) (2009) 9133–9140.
[75] R. Rockne, J.K. Rockhill, M. Mrugala, A.M. Spence, I. Kalet, K. Hendrickson, A. Lai, T. Cloughesy, E.C.A. Jr, K.R. Swanson, Predicting the efficacy of radiotherapy in individual glioblastoma patients in vivo: a mathematical modeling approach, Phys. Med. Biol. 55 (12) (2010) 3271.
[76] V.M. Pérez-García, M. Bogdanska, A. Martínez-González, J. Belmonte-Beitia, P. Schucht, L.A. Pérez-Romasanta, Delay effects in the response of low-grade gliomas to radiotherapy: a mathematical model and its therapeutical implications, Math. Med. Biol. 32 (3) (2015) 307–329.
[77] J.A. Weis, M.I. Miga, L.R. Arlinghaus, X. Li, A.B. Chakravarthy, V. Abramson, J. Farley, T.E. Yankeelov, A mechanically coupled reaction-diffusion model for predicting the response of breast tumors to neoadjuvant chemotherapy, Phys. Med. Biol. 58 (17) (2013) 5851.
[78] J.A. Weis, M.I. Miga, L.R. Arlinghaus, X. Li, V. Abramson, A.B. Chakravarthy, P. Pendyala, T.E. Yankeelov, Predicting the response of breast cancer to neoadjuvant therapy using a mechanically coupled reaction–diffusion model, Cancer Res. 75 (22) (2015) 4697–4707.
[79] J.A. Weis, M.I. Miga, T.E. Yankeelov, Three-dimensional image-based mechanical modeling for predicting the response of breast cancer to neoadjuvant therapy, Comput. Methods Appl. Mech. Engrg. 314 (2017) 494–512.
[80] E.A.B.F. Lima, J.T. Oden, D.A. Hormuth, T.E. Yankeelov, R.C. Almeida, Selection, calibration, and validation of models of tumor growth, Math. Models Methods Appl. Sci. 26 (12) (2016) 2341–2368.
[81] E.A.B.F. Lima, J.T. Oden, B. Wohlmuth, A. Shahmoradi, D.A. Hormuth, T.E. Yankeelov, L. Scarabosio, T. Horger, Selection and validation of predictive models of radiation effects on tumor growth based on noninvasive imaging data, Comput. Methods Appl. Mech. Engrg. 327 (Supplement C) (2017) 277–305.
[82] D.A. Hormuth, J.A. Weis, S.L. Barnes, M.I. Miga, E.C. Rericha, V. Quaranta, T.E. Yankeelov, A mechanically coupled reaction–diffusion model that incorporates intra-tumoural heterogeneity to predict in vivo glioma growth, J. R. Soc. Interface 14 (128) (2017).
[83] T.J.R. Hughes, J.A. Cottrell, Y. Bazilevs, Isogeometric analysis: CAD, finite elements, NURBS, exact geometry and mesh refinement, Comput. Methods Appl. Mech. Engrg. 194 (39–41) (2005) 4135–4195.
[84] J.A. Cottrell, T.J.R. Hughes, Y. Bazilevs, Isogeometric Analysis: Toward Integration of CAD and FEA, 2009.
[85] G. Lemaître, R. Martí, J. Freixenet, J.C. Vilanova, P.M. Walker, F. Meriaudeau, Computer-aided detection and diagnosis for prostate cancer based on mono and multi-parametric MRI: A review, Comput. Biol. Med. 60 (2015) 8–31.
[86] G. Lemaître, Computer-Aided Diagnosis for Prostate Cancer using Multi-Parametric Magnetic Resonance Imaging (Ph.D. thesis), Universitat de Girona and Université de Bourgogne, 2016.
[87] H. Gomez, K.G. van der Zee, Computational phase-field modeling, in: E. Stein, R. Borst, T.J.R. Hughes (Eds.), Encyclopedia of Computational Mechanics Second Edition, 2018, pp. 1–35.
[88] H. Gomez, M. Bures, A. Moure, A review on computational modelling of phase-transition problems, Phil. Trans. R. Soc. A 377 (2143) (2019) 20180203.
[89] F. Irgens, Continuum Mechanics, Springer, 2008.
[90] X. Chen, R.M. Summers, J. Yao, Kidney tumor growth prediction by coupling reaction-diffusion and biomechanical model, IEEE Trans. Biomed. Eng. 60 (1) (2013) 169–173.
[91] Y. Liu, S.M. Sadowski, A.B. Weisbrod, E. Kebebew, R.M. Summers, J. Yao, Patient specific tumor growth prediction using multimodal images, Med. Image Anal. 18 (3) (2014) 555–566.
[92] O. Clatz, M. Sermesant, P.Y. Bondiau, H. Delingette, S.K. Warfield, G. Malandain, N. Ayache, Realistic simulation of the 3-D growth of brain tumors in MR images coupling diffusion with biomechanical deformation, IEEE Trans. Med. Imaging 24 (10) (2005) 1334–1346.
[93] C. Hogea, C. Davatzikos, G. Biros, An image-driven parameter estimation problem for a reaction–diffusion glioma growth model with mass effects, J. Math. Biol. 56 (6) (2008) 793–825.
[94] P.J. De Visschere, A. Vral, G. Perletti, E. Pattyn, M. Praet, V. Magri, G.M. Villeirs, Multiparametric magnetic resonance imaging characteristics of normal, benign and malignant conditions in prostate, Eur. Radiol. 27 (5) (2017) 2095–2109.
[95] S.M. Noworolski, D.B. Vigneron, A.P. Chen, J. Kurhanewicz, Dynamic contrast-enhanced MRI and MR diffusion imaging to distinguish between glandular and stromal prostatic tissues, Magn. Reson. Imaging 26 (8) (2008) 1071–1080.
[96] A. Bharatha, M. Hirose, N. Hata, S.K. Warfield, M. Ferrant, K.H. Zou, E. Suarez-Santana, J. Ruiz-Alzola, A. D'Amico, R.A. Cormack, R. Kikinis, F.A. Jolesz, C.M. Tempany, Evaluation of three-dimensional finite element-based deformable registration of pre- and intraoperative prostate imaging, Med. Phys. 28 (12) (2001) 2551–2560.
[97] L. Zhai, J. Madden, W.-C. Foo, V. Mouraviev, T.J. Polascik, M.L. Palmeri, K.R. Nightingale, Characterizing stiffness of human prostates using acoustic radiation force, Ultrason. Imaging 32 (4) (2010) 201–213.

[98] Y. Wang, D. Ni, J. Qin, M. Xu, X. Xie, P.-A. Heng, Patient-specific deformation modelling via elastography: application to image-guided prostate interventions, Sci. Rep. 6 (2016) 27386.
[99] O. Rouvière, C. Melodelima, A. Hoang Dinh, F. Bratan, G. Pagnoux, T. Sanzalone, S. Crouzet, M. Colombel, F. Mège-Lechevallier, R. Souchon, Stiffness of benign and malignant prostate tissue measured by shear-wave elastography: a preliminary study, Eur. Radiol. 27 (5) (2017) 1858–1866.
[100] V. Gordon, M. Valentine, M. Gardel, D. Andor-Ardó, S. Dennison, A. Bogdanov, D. Weitz, T. Deisboeck, Measuring the mechanical stress induced by an expanding multicellular tumor system: a case study, Exp. Cell Res. 289 (1) (2003) 58–66.
[101] M.M. Lieber, T. Rhodes, D.J. Jacobson, M.E. McGree, C.J. Girman, S.J. Jacobsen, J.L. St. Sauver, Natural history of benign prostatic enlargement: long-term longitudinal population-based study of prostate volume doubling times, BJU Int. 105 (2) (2010) 214–219.
[102] C.G. Roehrborn, J. McConnell, J. Bonilla, S. Rosenblatt, P.B. Hudson, G.H. Malek, P.F. Schellhammer, R. Bruskewitz, A.M. Matsumoto, L.H. Harrison, et al., Serum prostate specific antigen is a strong predictor of future prostate growth in men with benign prostatic hyperplasia, J. Urol. 163 (1) (2000) 13–20.
[103] A.M. Williams, I. Simon, P.K. Landis, C. Moser, W. Christens-Barry, H.B. Carter, E.J. Metter, A.W. Partin, Prostatic growth rate determined from MRI data: Age-related longitudinal changes, J. Androl. 20 (4) (1999) 474–480.
[104] G. Lorenzo, M.A. Scott, K. Tew, T.J.R. Hughes, H. Gomez, Hierarchically refined and coarsened splines for moving interface problems, with particular application to phase-field models of prostate tumor growth, Comput. Methods Appl. Mech. Engrg. 319 (2017) 515–548.
[105] T.J.R. Hughes, The Finite Element Method: Linear Static and Dynamic Finite Element Analysis, Dover Publications, 2000.
[106] L.A. Piegl, W. Tiller, The NURBS Book (Monographs in Visual Communication), Springer, 1996.
[107] Y. Bazilevs, V.M. Calo, J.A. Cottrell, J.A. Evans, T.J.R. Hughes, S. Lipton, M.A. Scott, T.W. Sederberg, Isogeometric analysis using T-splines, Comput. Methods Appl. Mech. Engrg. 199 (5) (2010) 229–263.
[108] I. Akkerman, Y. Bazilevs, V.M. Calo, T.J.R. Hughes, S. Hulshoff, The role of continuity in residual-based variational multiscale modeling of turbulence, Comput. Mech. 41 (3) (2008) 371–378.
[109] J. Chung, G. Hulbert, A time integration algorithm for structural dynamics with improved numerical dissipation: the generalized-α method, J. Appl. Mech. 60 (2) (1993) 371–375.
[110] K.E. Jansen, C.H. Whiting, G.M. Hulbert, A generalized-α method for integrating the filtered Navier–Stokes equations with a stabilized finite element method, Comput. Methods Appl. Mech. Engrg. 190 (3–4) (2000) 305–319.
[111] Y. Saad, M.H. Schultz, GMRES: A generalized minimal residual algorithm for solving nonsymmetric linear systems, SIAM J. Sci. Stat. Comput. 7 (3) (1986) 856–869.
[112] H. Gómez, V.M. Calo, Y. Bazilevs, T.J.R. Hughes, Isogeometric analysis of the Cahn-Hilliard phase-field model, Comput. Methods Appl. Mech. Engrg. 197 (49–50) (2008) 4333–4352.
[113] Y.J. Zhang, Geometric Modeling and Mesh Generation from Scanned Images, in: Chapman & Hall/CRC Mathematical and Computational Imaging Sciences Series, Chapman and Hall/CRC, 2016.
[114] B. Urick, T.M. Sanders, S.S. Hossain, Y.J. Zhang, T.J.R. Hughes, Review of patient-specific vascular modeling: Template-based isogeometric framework and the case for CAD, Arch. Comput. Methods Eng. (2017) 1–24.
[115] M.S. Floater, K. Hormann, Surface parameterization: a tutorial and survey, in: N.A. Dodgson, M.S. Floater, M.A. Sabin (Eds.), Advances in Multiresolution for Geometric Modelling, Springer Berlin Heidelberg, Berlin, Heidelberg, 2005, pp. 157–186.
[116] Y. Zhang, W. Wang, T.J.R. Hughes, Solid T-spline construction from boundary representations for genus-zero geometry, Comput. Methods Appl. Mech. Engrg. 249 (2012) 185–197.
[117] G. Lorenzo, Tissue-Scale, Patient-Specific Modeling and Simulation of Prostate Cancer Growth (Ph.D. thesis), Universidade da Coruña, 2018.
[118] A. Fedorov, R. Beichel, J. Kalpathy-Cramer, J. Finet, J.-C. Fillion-Robin, S. Pujol, C. Bauer, D. Jennings, F. Fennessy, M. Sonka, J. Buatti, S. Aylward, J.V. Miller, S. Pieper, R. Kikinis, 3D slicer as an image computing platform for the quantitative imaging network, Magn. Reson. Imaging 30 (9) (2012) 1323–1341.
[119] P. Cignoni, M. Callieri, M. Corsini, M. Dellepiane, F. Ganovelli, G. Ranzuglia, Meshlab: an open-source mesh processing tool, in: V. Scarano, R.D. Chiara, U. Erra (Eds.), Eurographics Italian Chapter Conference, The Eurographics Association, 2008.
[120] U. Ayachit, The ParaView Guide (Full Color Version): A Parallel Visualization Application, Kitware, Incorporated, 2015.
[121] A.W. Partin, H.B. Carter, D.W. Chan, J.I. Epstein, J.E. Oesterling, R.C. Rock, J.P. Weber, P.C. Walsh, Prostate specific antigen in the staging of localized prostate cancer: influence of tumor differentiation, tumor volume and benign hyperplasia, J. Urol. 143 (4) (1990) 747–752.
[122] B. Turkbey, H. Mani, O. Aras, A.R. Rastinehad, V. Shah, M. Bernardo, T. Pohida, D. Daar, C. Benjamin, Y.L. McKinney, W.M. Linehan, B.J. Wood, M.J. Merino, P.L. Choyke, P.A. Pinto, Correlation of magnetic resonance imaging tumor volume with histopathology, J. Urol. 188 (4) (2012) 1157–1163.
[123] C.M. Moore, N.L. Robertson, F. Jichi, A. Damola, G. Ambler, F. Giganti, A.J. Ridout, S.R. Bott, M. Winkler, H.U. Ahmed, et al., The effect of dutasteride on magnetic resonance imaging defined prostate cancer: MAPPED—A randomized, placebo controlled, double-blind clinical trial, J. Urol. 197 (4) (2017) 1006–1013.
[124] A. Goriely, The Mathematics and Mechanics of Biological Growth (Interdisciplinary Applied Mathematics), Springer, 2017.
[125] A. Menzel, E. Kuhl, Frontiers in growth and remodeling, Mech. Res. Commun. 42 (2012) 1–14.
[126] L.M. Johnson, B. Turkbey, W.D. Figg, P.L. Choyke, Multiparametric MRI in prostate cancer management, Nature Rev. Clin. Oncol. 11 (6) (2014) 346–353.